8-2015

Empirical Measurement and Model Validation of Infrared Spectra of Contaminated Surfaces

Sean Archer

Empirical Measurement and Model Validation of Infrared Spectra of Contaminated Surfaces

by

Sean Archer

B.S. Meteorology, The College at Brockport, 2013

A thesis submitted in partial fulfillment of the
requirements for the degree of Master of Science
in the Chester F. Carlson Center for Imaging Science
College of Science
Rochester Institute of Technology

August 2015

Signature of the Author _____

Accepted by _____
Coordinator, M.S. Degree Program Date

CHESTER F. CARLSON CENTER FOR IMAGING SCIENCE
COLLEGE OF SCIENCE
ROCHESTER INSTITUTE OF TECHNOLOGY
ROCHESTER, NEW YORK

CERTIFICATE OF APPROVAL

M.S. DEGREE THESIS

The M.S. Degree Thesis of Sean Archer
has been examined and approved by the
thesis committee as satisfactory for the
thesis required for the
M.S. degree in Imaging Science

Dr. John Kerekes, Thesis Advisor

Dr. Michael Gartley

Dr. Carl Salvaggio

Date

Empirical Measurement and Model Validation of Infrared Spectra of Contaminated Surfaces

by

Sean Archer

Submitted to the
Chester F. Carlson Center for Imaging Science
in partial fulfillment of the requirements
for the Master of Science Degree
at the Rochester Institute of Technology

Abstract

The goal of this thesis was to validate predicted infrared spectra of liquid contaminated surfaces from a micro-scale bi-directional reflectance distribution function (BRDF) model through the use of empirical measurement. Liquid contaminated surfaces generally require more sophisticated radiometric modeling to numerically describe surface properties. The Digital Image and Remote Sensing Image Generation (DIRSIG) model utilizes radiative transfer modeling to generate synthetic imagery for a variety of applications. Aside from DIRSIG, a micro-scale model known as microDIRSIG has been developed as a rigorous ray tracing physics-based model that could predict the BRDF of geometric surfaces that are defined as micron to millimeter resolution facets. The model offers an extension from the conventional BRDF models by allowing contaminants to be added as geometric objects to a micro-facet surface.

This model was validated through the use of Fourier transform infrared spectrometer measurements. A total of 18 different substrate and contaminant combinations were measured and compared against modeled outputs. The substrates used in this experiment were wood and aluminum that contained three different paint finishes. The paint finishes included no paint, Krylon ultra-flat black, and Krylon glossy black. A silicon based oil

(SF96) was measured out and applied to each surface to create three different contamination cases for each surface. Radiance in the longwave infrared region of the electromagnetic spectrum was measured by a Design and Prototypes (D&P) Fourier transform infrared spectrometer and a Physical Sciences Inc. Adaptive Infrared Imaging Spectroradiometer (AIRIS).

The model outputs were compared against the measurements quantitatively in both the emissivity and radiance domains. A temperature emissivity separation (TES) algorithm had to be applied to the measured radiance spectra for comparison with the microDIRSIG predicted emissivity spectra. The model predicted emissivity spectra was also forward modeled through a DIRSIG simulation for comparisons to the radiance measurements. The results showed a promising agreement for homogeneous surfaces with liquid contamination that could be well characterized geometrically. Limitations arose in substrates that were modeled as homogeneous surfaces, but had spatially varying artifacts due to uncertainties with contaminant and surface interactions. There is high desire for accurate physics based modeling of liquid contaminated surfaces and this validation framework may be extended to include a wider array of samples for more realistic natural surfaces that are often found in real world scenarios.

Acknowledgements

I would like to start off by thanking my thesis advisor Dr. John Kerekes for his consistent support, feedback, and guidance over the course of the last two years. This thesis also would not have been possible without the support of my research committee. Thank you to Dr. Michael Gartley for always answering my sometimes "not so intelligent" questions and willingness to take time out his day to help me understand certain phenomenology. I would also like to thank Dr. Carl Salvaggio for his expertise in the field measurement aspect of this research. It has been an exciting, busy, and stressful at times two years and I am very grateful for all the contributions my professors and the staff at the Center for Imaging Science made to provide me with a world class education in Imaging Science. I would also like to thank my parents Geralyn and John for always believing in me and allowing me to pursue my interests. I can't express enough how thankful I am for all the sacrifices they have made over the years.

Portions of this work were supported in part by Physical Sciences Inc. and the US Army under Subcontract NO. SC60721-1811-001 and Contract NO. W911SR-13-C-0005. Any opinions, findings and conclusions or recommendations expressed in this material are those of the authors and do not necessarily reflect the views to the US Army.

Contents

List of Figures

List of Tables

Chapter 1

Introduction and Objectives

1.1 Introduction

Remote sensing, in a broad sense, can be described as the field of study associated with extracting information about an object without coming into physical contact with it [1]. Within that context, remote sensing encompasses a vast amount of applications within vision, astronomy, medical imaging, and Earth observation. Earth observation by airborne or space-based remote sensing systems has grown considerably since World War I, and has provided invaluable information regarding military intelligence, environmental monitoring, and disaster relief.

Earth remote sensing systems function by detecting and processing electromagnetic energy that may naturally leave an object (passive) or be reflected off an object by active illumination (active). System technology has evolved considerably from monochrome film cameras to hyperspectral digital systems that can provide fine spectral resolution across the visible to the long wave infrared regions of the electromagnetic spectrum. Hyperspectral systems have exponentially expanded the field to include applications such as material identification or target detection based on unique spectral surface properties that may be extracted from the recorded electromagnetic energy.

Sensor reaching radiance in the thermal infrared is typically comprised of self emitted photons directly from the target, photons emitted from the background or atmosphere that reflect off the target to the sensor, and photons that are emitted directly from the atmosphere. The sensor reaching radiance is typically a function of wavelength or frequency and hyperspectral systems generally contain hundreds of narrow contiguous spectral bands. Several spectral algorithms have been developed to provide a means for identifying materials or targets based on unique spectral features. Often, the surface optical properties reflectivity and emissivity are sought after and accurate extraction of these parameters typically requires system calibration and a thorough understanding of the atmospheric effects on the sensor reaching radiance.

The sensor reaching radiance, and subsequently, the optical properties are also a function of the viewing angle of the sensor. Many materials reflect or emit energy differently as the viewing angle changes and spectral algorithms may need to account for the bidirectional reflectance distribution function (BRDF). Measuring the BRDF often requires several measurements and then interpolation which is typically not feasible for real world applications. Therefore, physics based BRDF models have been developed for approximating the BRDF. Several BRDF models exist and have provided accurate BRDF predictions when compared to laboratory BRDF measurements for pristine surfaces.

In the real world, materials are rarely pristine and often contain some form of contamination. The presence of a contaminant can significantly alter a material's spectra and lead to erroneous results for material characterization or target detection algorithms. An advanced reverse ray tracing BRDF model (microDIRSIG) has been developed to predict the BRDF of contaminated surfaces that are well defined optically and geometrically [18]. While microDIRSIG has produced promising results for simple simulations when comapred to empirical databases, there is currently not a framework in place for a full validation of the BRDF model in more complex and realistic contamination scenarios. This thesis work is meant to provide the next step in model validation by providing accurate field

measurements of well characterized contaminated surfaces for quantitative comparison.

1.2 Objectives

The primary objective of this work is to verify and validate predicted infrared spectra of contaminated surfaces from a microfaceted thermal bidirectional reflectance distribution model through the use of empirical measurements. Specific tasks include:

1. Design and prepare empirical experiments of contaminated surfaces that may be replicated with current modeling capabilities.
2. Conduct accurate and reliable thermal measurements using Fourier transform interferometer instruments.
3. Process data accordingly and assess the accuracy and confidence within the processed measured data.
4. Quantitatively compare measurements against model predicted outputs to determine the accuracy of the model and explain potential limitations of the current modeling capabilities.

1.3 Thesis Overview and Organization

Chapter 2 provides an introductory overview of how electromagnetic radiation is characterized and how it propagates from its source to a detector. The following chapter (3) gives an overview of prior work and recent advancements in measuring BRDF, measuring the effects of contaminants, the advances of microDIRSIG, and prior validation techniques for microDIRSIG.

Chapter 4 provides context on the empirical measurement process and gives a detailed

description of experimentation and processing techniques. This chapter is followed up with results from this experiment and a quantitative comparison to the predicted model outputs.

Finally, chapter 6 summarizes the results and discusses future work. This chapter outlines some of the potential limitations that arose within the model validation and offers considerations for future work in expanding the model validation.

Chapter 2

Theory and Background

This chapter provides an introductory description of electromagnetic radiation and and how it interacts with matter. Section 2.1 describes the properties of electromagnetic radiation and how it may be described at the boundaries of different optical media. Section 2.2 extends the principles covered in the previous section and provides context as to how electromagnetic radiation interacts with real world materials. Section 2.3 then introduces the bi-directional reflectance distribution function and how physics based models may describe how electromagnetic radiation scatters upon striking a surface. Finally, section 2.4 introduces infrared radiometry and discusses the potential sources of electromagnetic radiation that a sensor may detect.

2.1 Electromagnetics

Since the 17th century, the physical understanding of light has been a very perplexing and fascinating topic in the history of science. Light, which can be characterized by its wavelength, amplitude, and polarization state, has been viewed as a particle and wave throughout history. In the 17th century, Isaac Newton was the most prominent advocate of a particle theory and regarded rays of light as streams of very small particles emitted

from a source of light and traveling in straight lines [2].

Also during this time period, a Dutch scientist Christian Huygens viewed light as a wave after he experimentally found that two intersecting beams of light emerged unmodified similarly to the case of two water or sound waves. The wave theory began to gain more scientific merit when Englishman Thomas Young performed the double slit experiment. This experiment was set up by illuminating an opaque plate with two small, closely spaced openings by a monochromatic light source. Young observed a complex interference pattern similar to water waves on the screen beyond the plate [2].

As time progressed toward the 20th century, scientific confidence of the wave theory continued to increase. Results of experiments executed by Augustin Fresnel, which required light to be assumed a transverse wave, led to the derivations of the Fresnel equations. The Fresnel equations describe what fraction of light is reflected and refracted (transmitted), as well as the phase shift, when light enters a second medium.

Advances in the field of electricity and magnetism from physicists such as Michael Faraday, Carl Friedrich Gauss, Charles-Augustin de Coulomb, and Andre-Marie Ampere provoked James Clerk Maxwell to further investigate light and discover that light was a form of radiation containing an electric and magnetic field propagating through free space at a constant velocity. Maxwell proposed that the speed of light c could be represented by

$$c = \frac{1}{\sqrt{\epsilon_0 \mu_0}}, \tag{2.1}$$

where ϵ_0 defines the permittivity and μ_0 defines the permeability of free space [2]. He later derived four equations that essentially provide the framework for the field of classical electrodynamics and optics.

The solution to Maxwell's equation can be described by electromagnetic radiation (EMR) in the general form

$$\overrightarrow{E}(z,t) = \overrightarrow{E_0} \mathrm{e}^{i(\omega t + \overrightarrow{k} \cdot \overrightarrow{z} + \phi)}, \tag{2.2}$$

where E_0 represents the amplitude and the direction of the electric field as a function of position, z and time, t. The angular frequency is given by ω and the wave vector is represented by $\overrightarrow{k}$. The angular frequency and wave vector are related by

$$|k| = \frac{\omega}{c} = \frac{2\pi}{\lambda}, \tag{2.3}$$

where λ is the wavelength of light and c, as defined above, represents the speed of light as it propagates through a vacuum. The phase shift or wave offset is represented by ϕ. Upon Maxwell's discoveries, light is now viewed as a particular region of the electromagnetic spectrum that is differentiated by its wavelength. The invention of dispersive optical systems led to the field of spectroscopy where electromagnetic radiation can be viewed as a function of wavelength.

2.1.1 Electromagnetic Radiation at Boundaries

The propagation characteristics of electromagnetic radiation at media boundaries are largely dependent on the optical properties of both mediums. The behavior of an electromagnetic wave as it propagates through a medium can be described by the index of refraction, n, which can be represented by

$$n = \sqrt{\frac{\epsilon\mu}{\epsilon_0\mu_0}}, \tag{2.4}$$

where ϵ and μ represent the permittivity and permeability of the media. It may be seen that from (2.1), that the refractive index is a ratio of the velocity of the wave in free space compared to the velocity in the media. The index of refraction is often a complex quantity that is frequency dependent and written in the form

$$\tilde{n} = n - i\kappa \tag{2.5}$$

where n is defined in (2.4) and κ is the extinction coefficient.

Direction

The simple law of reflectance states that when light strikes a surface, the angle of incidence, θ_i is equal to the angle of reflectance, θ_r. If this surface, or change in medium is tranmissive, the light propagates through the boundary and the angle of transmittance, θ_t is given by Snell's law of refraction which states

$$\tilde{n_i} sin(\theta_i) = \tilde{n_t} sin(\theta_t) \tag{2.6}$$

Snell's law provides insight on an interesting phenomenon known as *total internal reflection*. This situation occurs when light propagates through a boundary in which $\tilde{n_i}$ is significantly higher than $\tilde{n_t}$. At this high-to-low interface, a critical angle exists where light will no longer transmit through the interface and is perfectly reflected. The critical angle can be computed by

$$\theta_c = sin^{-1}(\frac{\tilde{n_i}}{\tilde{n_t}}). \tag{2.7}$$

Magnitude

The magnitude of the reflected and transmitted waves is also a function of the complex indices of refraction of both mediums. The Fresnel equations can express the magnitude of the electric field in two orthogonal components relative to the plane of incidence for the reflected and transmitted light. These components are known as s-polarization and p-polarization and represent the components of the electric field that are perpendicular or parallel to the plane of incidence respectively. The orientation of the waves is referred to as the polarization and is discussed in detail later.

The magnitude of the s and p polarization components can be written as

$$r_s(\theta_i) = \frac{2\tilde{n_i} cos(\theta_i)}{\tilde{n_i} cos(\theta_i) + \sqrt{\tilde{n_t}^2 - \tilde{n_i}^2 sin^2(\theta_i)}} \tag{2.8}$$

$$r_p(\theta_i) = \frac{2\tilde{n_i}\tilde{n_t} cos(\theta_i)}{\tilde{n_t}^2 cos(\theta_i) + \tilde{n_i}\sqrt{\tilde{n_t}^2 - \tilde{n_i}^2 sin^2(\theta_i)}} \tag{2.9}$$

$$t_s(\theta_i) = \frac{\tilde{n_i} cos(\theta_i) - \sqrt{\tilde{n_t}^2 - \tilde{n_i}^2 sin^2(\theta_i)}}{\tilde{n_i} cos(\theta_i) - \sqrt{\tilde{n_t}^2 + \tilde{n_i}^2 sin^2(\theta_i)}} \tag{2.10}$$

$$t_p(\theta_i) = \frac{\tilde{n_t}^2 cos(\theta_i) - \tilde{n_i}\sqrt{\tilde{n_t}^2 - \tilde{n_i}^2 sin^2(\theta_i)}}{\tilde{n_i}^2 cos(\theta_i) + \tilde{n_i}\sqrt{\tilde{n_t}^2 + \tilde{n_i}^2 sin^2(\theta_i)}} \tag{2.11}$$

where the r_s and r_p terms represent the magnitude of the reflected waves and t_s and t_p represent the magnitude of the transmitted waves. Here the transmission angle, θ_t has been replaced by $\sqrt{\tilde{n_t}^2 - \tilde{n_i}^2 sin^2(\theta_i)}$ from Snell's law.

In remote sensing, the quantity typically measured is the irradiance incident on the detector which represents the square of the electric field. The above quantities represent the magnitudes of the electric field and therefore need to be represented by

$$\rho_s = r_s^2 \tag{2.12}$$

$$\rho_p = r_p^2 \tag{2.13}$$

$$\tau_s = t_s^2 \tag{2.14}$$

$$\tau_p = t_p^2 \tag{2.15}$$

where reflectance is denoted by ρ and transmission is τ. Typically, the incident light is propagating through air where $\tilde{n_i} \approx 1 + i0$ and the permeability of the air and target material are essentially the same. With these two assumptions, the Fresnel equations for reflected energy can be written as

$$\rho_s(\theta_i) = \frac{(A - cos(\theta_i))^2 + B^2}{(A + cos(\theta_i))^2 + B^2} \tag{2.16}$$

$$\rho_p(\theta_i) = \rho_s \frac{(A - sin(\theta_i)tan(\theta_i))^2 + B^2}{(A + sin(\theta_i)tan(\theta_i))^2 + B^2} \tag{2.17}$$

where the quantities A and B correspond to

$$A = \sqrt{\frac{\sqrt{4n^2\kappa^2 + (n^2 - \kappa^2 - sin^2(\theta_i))^2} + n^2 - \kappa^2 - sin^2(\theta_i)}{2}} \tag{2.18}$$

$$B = \sqrt{\frac{\sqrt{4n^2\kappa^2 + (n^2 - \kappa^2 - sin^2(\theta_i))^2} - n^2 + \kappa^2 + sin^2(\theta_i)}{2}}. \tag{2.19}$$

These equations separate the complex index of refraction, $\tilde{n}$ into the phase velocity, n and absorption, κ components. The total reflectance, R_{TOT} of the unpolarized light is the average of the individual polarized components

$$R_{TOT} = \frac{\rho_s + \rho_p}{2} \tag{2.20}$$

2.1.2 Polarization

Polarization was defined earlier as the orientation of the oscillating electric field perpendicular to the direction of travel, $\hat{z}$. This information may be obtained by treating the irradiance, $\overrightarrow{E}$, incident on the detector as a vector with $\hat{x}, \hat{y}$ components that are perpendicular to the direction of propagation.

Polarization may be classified as linear, circular, or elliptical depending on the phase difference of the $\hat{x}, \hat{y}$ components. When $\hat{x}$ and $\hat{y}$ oscillate completely in phase, the light is said to be linearly polarized. If these components oscillate with the same amplitude but 90 degrees out of phase, the light is considered to be circularly polarized. Any other phase difference causes an elliptical polarization. Polarization is often described by using a four element vector known as a Stokes vector.

Stokes Vectors

Stokes vectors were developed as a method for describing the polarization state of incident incoherent radiation. The polarization state is defined relative to a reference plane which is typically the surface under the observation, such as Earth's surface. In section 2.1.1, the concepts of the s and p polarization were introduced in discussion of the Fresnel coefficients. The s polarization defines the $x = 0$ degree orientation and the $\hat{x}$ component of the electric field, E_x. The p polarization similarly defines the E_y component where there is an $x = \pm 90$ degree orientation.

The electromagnetic wave equation can be expanded in terms of the magnitude and

phase of the $\hat{x}, \hat{y}$ components of the electric field

$$\overrightarrow{E}(z,t) = (E_{0x}e^{i\delta_x}\hat{x} + E_{0y}e^{i\delta_y}\hat{y})e^{i(\omega t - \overrightarrow{k}\cdot\overrightarrow{z})} \tag{2.21}$$

where δ represents the phase. The Stokes vectors can then be defined as

$$\begin{bmatrix} S_0 \\ S_1 \\ S_2 \\ S_3 \end{bmatrix} = \begin{bmatrix} \langle E_{0x}^2 + E_{0y}^2 \rangle \\ \langle E_{0x}^2 - E_{0y}^2 \rangle \\ \langle 2E_{0x}E_{0y}cos\delta \rangle \\ \langle 2E_{0x}E_{0y}sin\delta \rangle \end{bmatrix}. \tag{2.22}$$

Stokes vectors are often normalized by dividing the elements by S_0. The S_0 element contains the unpolarized electromagnetic radiation incident onto the detector and is proportional to the square of the electric field. The S_1 element represents the difference of the $\hat{x}$ and $\hat{y}$ components and gives information about which direction is more polarized. This value ranges from -1 to 1 depending on how polarized the field is in the $\hat{x} = 0$ and $\hat{y} = 90$ directions respectively. The S_2 component contains information about the 45° and 135° directions which can be defined as the $\hat{a}$ and $\hat{b}$ directions. Positive values indicates more polarization in the $\hat{a}$ direction and a negative value indicate more polarization in the $\hat{b}$ direction. The S_3 component indicates the circular polarization where positive values correspond to a more left circular state and negatives values correspond to a right circular polarization.

Stokes vectors may also be used to define polarization relationships such as *degree of polarization*(DOP) and *degree of linear polarization*(DOLP) which provide percentages of how polarized the light is. Coherent light has a DOP equal to 100% while incoherent has DOP $<$ 100%. The DOP and DOLP may be written as

$$DOP = \frac{\sqrt{S_1^2 + S_2^2 + S_3^2}}{S_0} \tag{2.23}$$

$$DOLP = \frac{\sqrt{S_1^2 + S_2^2}}{S_0}. \tag{2.24}$$

Mueller Matrices

Mueller calculus is a method of manipulating Stokes vectors to define how polarized light is transferred through a medium. The magnitude and polarization of light as it travels through a medium can change based on the transmissive and reflective properties of the medium, which stem back from the Fresnel equation. Mueller matrices, M were developed as a transfer function to describe these changes in radiant flux. The general form of Mueller calculus can be represented by

$$\overrightarrow{S}_{out} = M\overrightarrow{S}_{in}. \tag{2.25}$$

A Mueller matrix is a $4x4$ matrix that replaces scalar transmission and reflectivity values with directional information and is generically given by

$$M = \begin{pmatrix} m_{0,0} & m_{1,0} & m_{2,0} & m_{3,0} \\ m_{0,1} & m_{1,1} & m_{2,1} & m_{3,1} \\ m_{0,2} & m_{1,2} & m_{2,2} & m_{3,2} \\ m_{0,3} & m_{1,3} & m_{2,3} & m_{3,3}. \end{pmatrix} \tag{2.26}$$

The Mueller matrices presented below are considered ideal linear polarization filters. Here we represent the filters at 0°, 90°, 45°, and 135° by

$$M(0^\circ) = \frac{1}{2}\begin{pmatrix} 1 & 1 & 0 & 0 \\ 1 & 1 & 0 & 0 \\ 0 & 0 & 0 & 0 \\ 0 & 0 & 0 & 0 \end{pmatrix}, \tag{2.27}$$

$$M(90^\circ) = \frac{1}{2}\begin{pmatrix} 1 & -1 & 0 & 0 \\ -1 & 1 & 0 & 0 \\ 0 & 0 & 0 & 0 \\ 0 & 0 & 0 & 0 \end{pmatrix}, \tag{2.28}$$

$$M(45^\circ) = \frac{1}{2}\begin{pmatrix} 1 & 0 & 1 & 0 \\ 0 & 0 & 0 & 0 \\ 1 & 0 & 1 & 0 \\ 0 & 0 & 0 & 0 \end{pmatrix}, \tag{2.29}$$

$$M(135^\circ) = \frac{1}{2}\begin{pmatrix} 1 & 0 & -1 & 0 \\ 0 & 0 & 0 & 0 \\ -1 & 0 & 1 & 0 \\ 0 & 0 & 0 & 0 \end{pmatrix}. \tag{2.30}$$

If the polarizer is oriented at any other angle,θ, the Mueller matrix may be represented by

$$M(\theta) = \frac{1}{2}\begin{pmatrix} 1 & cos(2\theta) & sin(2\theta) & 0 \\ cos(2\theta) & cos^2(2\theta) & cos(2\theta)sin(2\theta) & 0 \\ sin(2\theta) & cos(2\theta)sin(2\theta) & sin^2(2\theta) & 0 \\ 0 & 0 & 0 & 0 \end{pmatrix}. \tag{2.31}$$

2.2 Surface Reflectance and Emission

We have now defined electromagnetic radiation and discussed the parameters that describe the physical properties of light. In many remote sensing applications, the primary parameters of interest are the surface or target reflectance, transmission, and absorption properties. The previous section introduced the Fresnel equations which determined the reflectance magnitude from the optical properties of materials and the angle of incidence. The direction of the reflected energy was also characterized by the simple law of reflection where $\theta_r = \theta_i$. These laws however, do not accurately depict the reflectance properties of real man-made materials that are significantly more complex.

2.2.1 Real World Reflection

In theory, the Fresnel equations assume perfectly planar "mirror" surfaces where all incident energy is reflected in the $\theta_r = \theta_i$ or specular direction. This assumption is not valid for most man made materials, however almost-flat surfaces such as still water, glass, or glossy paints can be accurately modeled by the Fresnel equations. The opposite of a specular surface is a Lambertian or ideal diffuse surface where the incident light is reflected in all directions evenly. Surfaces built from non-absorbing powders or fibers such as plaster or paper reflect light at an almost ideal diffuse efficiency. Most materials exhibit a mixture of diffuse and specular reflection which is largely dependent on the surface properties [1].

Surface roughness and internal scattering are the two main reasons why light is reflected outside of the specular direction. Surface roughness leads to varying distribution of surface orientation and each facet will reflect the incident energy at a different angle. This roughness can vary on several different scales depending on the material. Some materials may even have varying scales of surface roughness such as a desert which has millimeter scale roughness from individual sand particles and meter roughness due to the elevation of sand dunes. A smooth surface is required to produce specular reflection however a rough surface is not required to produce diffuse reflection.

Internal scattering, also known as volumetric scattering is the main contributor to non-specular reflection and occurs when light undergoes multiple internal reflection events upon entering a material. The multiple direction changes leads to a random distribution of light exiting the surface at varying intensities and directions. This is a complex interaction and a photon can take several different paths and undergo several different scattering events before finally reaching the detector. The random nature of light exiting the surface also evokes a random or unpolarized orientation. A detailed figure showing this complex interaction is shown in Figure 2.1 [3].

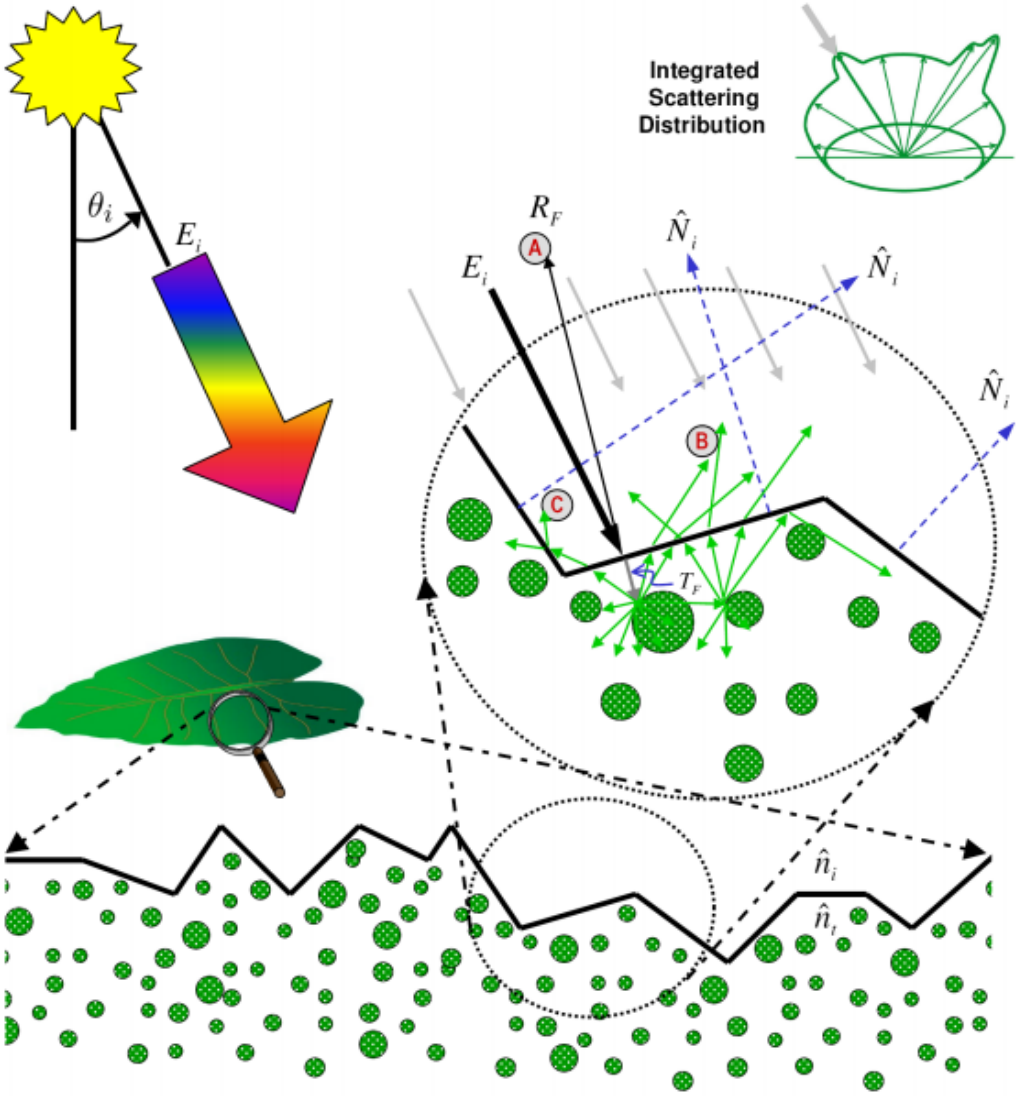

Figure 2.1: Detailed view of light scatter from material. From Shell [3]

2.3 Bidirectional Reflectance Distribution Function

Characterizing the directional nature of light scatter off of surfaces is a very common problem within the remote sensing community. Optical scatter from surfaces may be any combination of specular or diffuse reflectance. The bidirectional reflectance distribution function is a common metric used to describe the optical scatter of light from surfaces [1]. The BRDF describes the fractional amount of exiting light that is scattered off a material into any angular direction within the hemisphere above. Specular, or almost specular surfaces such as a mirror show a high forward scattering peak at a reflectance angle equal to the incident angle with respect to the normal. A diffuse surface, such as the white painted drywall in an office will show an even hemispherical distribution. Figure 2.2 shows an example of BRDF distributions for the ideal specular and diffuse situations, as well as possible combinations of diffuse and specular reflectance typically seen in real world applications.

The BRDF, $\rho(\theta_i, \phi_i, \theta_r, \phi_r, \lambda)$ is a spectral function of the incident and reflected angles and can be defined as the ratio of reflected radiance, $dL(\theta_r, \phi_r, \lambda)$ and the incident irradiance, $dE(\theta_i, \phi_i, \lambda)$ or

$$\rho(\theta_i, \phi_i, \theta_r, \phi_r, \lambda) = \frac{dL(\theta_r, \phi_r, \lambda)}{dE(\theta_i, \phi_i, \lambda)}. \tag{2.32}$$

Here the exiting radiance is in units of $\frac{W}{m^2 sr \mu m}$ and the incident irradiance is in units of $\frac{W}{m^2 \mu m}$ which upon cancellation results in overall units of inverse steradians, sr^{-1}. The nomenclature and geometry of the BRDF is important to define and crucial in understanding the BRDF. Nicodemus [4] recommended a standard nomenclature that is used in many BRDF models today. Most materials exhibit azimuthal or rotational symmetry around a surface normal. This assumption allows for the BRDF to be simplified by characterizing the ϕ_i and ϕ_r as the difference between them, $\Delta\phi$. Therefore, the incident azimuth angle can be assume to equal 0° and the BRDF can be rewritten as $\rho(\theta_i, \theta_r, \phi, \lambda)$. The labeled geometry is shown in Figure 2.3.

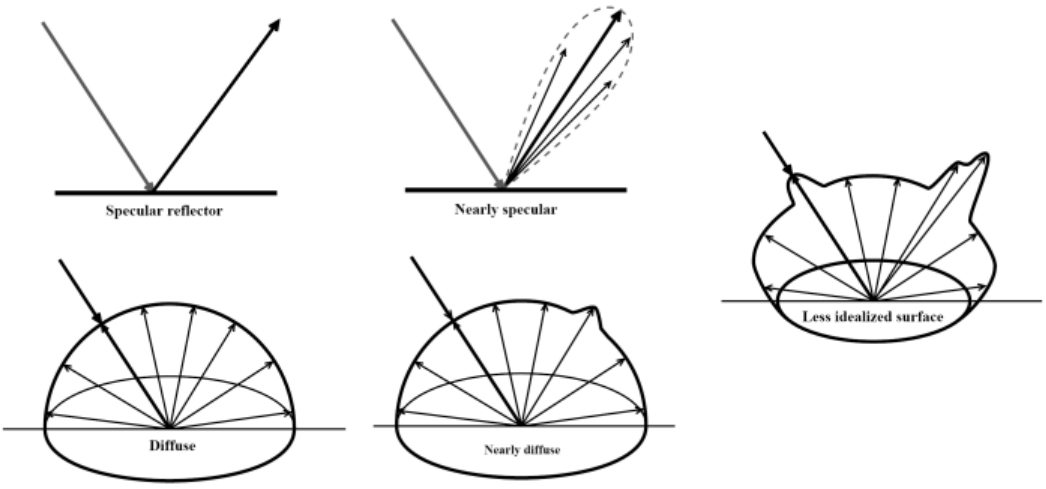

Figure 2.2: Examples of BRDF distributions for specular and diffuse (left) materials and more realistic materials (right). From Schott [1]

Another quantity of interest is the directional hemispherical reflectance (DHR) which is defined as the integral of the BRDF over all viewing angles for a specified incident angle. The DHR is a function of the incident zenith angle, incident azimuth angle, and the wavelength and may be written as

$$\rho_{DHR}(\theta_i, \phi_i, \lambda) = \int_0^{2\pi} \int_0^{\pi/2} \rho(\theta_i, \theta_r, \Delta\phi, \lambda) cos\theta_r sin\theta_r d\theta_r d\phi_r, \tag{2.33}$$

where the integration bounds account for the entire hemisphere above the sample. For ideal diffuse surfaces, the BRDF in terms of the DHR is a very simple expression represented by

$$\rho(\theta_i, \theta_r, \Delta\phi, \lambda) = \rho(\lambda) = \frac{\rho_{DHR}}{\pi} \tag{2.34}$$

The DHR may also be represented in terms of the emissivity, which is typically the parameter of interest in the thermal infrared. If the transmission of the material is assumed

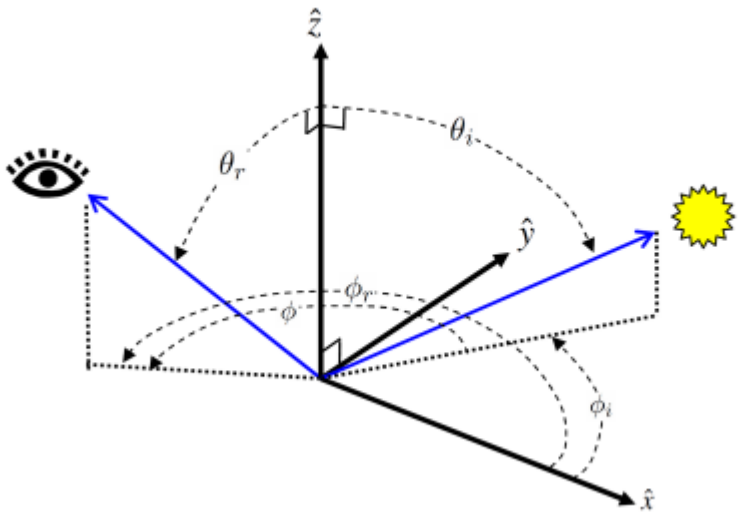

Figure 2.3: Geometry of the BRDF, which is specified by the source and reflected zenith and azimuth angles. Figure from [3]

to be zero, then Kirchoff's law allows us to define the emissivity as

$$\epsilon(\theta_i, \lambda) = 1 - \rho_{DHR}(\theta_i, \lambda) \tag{2.35}$$

The BRDF is difficult to measure for several reasons. Complete data sets can be very large because BRDF is not only a function of $\theta_i, \theta_r, \phi_i, \phi_r$, and wavelength, but also source and detector polarization, material, temperature, and surface conditions such as texture or roughness [6]. Measurements can also be very expensive, time consuming, and difficult to consistently and accurately conduct for multiple materials. Instruments such as goniometers may be able to efficiently take measurements at most zenith and azimuth angles, however limitations typically arise due to instrument design. A fully quantified BRDF derived from empirical measurement would also require an interpolation or extrapolation of often sparse hemispherical sampled data. Reflectance measurements are also much less accurate at near grazing angles because many man made materials become almost specu-

lar when $\theta_i > 80°$.

Several mathematical models have been developed to characterize the BRDF. Some BRDF models rely on solely empirical measurement where several measurements at an adequate hemispherical sampling is required for accurate interpolation. Physical BRDF models are initialized by parameters that describe the materials surface properties and follow the fundamentals of first-principle physics where electromagnetic energy is numerically propagated through material interactions. Semi-empirical models employ both physics-based principles and are driven by some measured data. The following sub-sections introduce some of the more commonly used BRDF models in remote sensing applications. These models can provide valuable insight on material reflectance properties when measurements are not feasible or when limitations within the measurements arise. BRDF is represented as the variable f with subscripts denoting the specific model in the following sub-sections.

2.3.1 Torrance-Sparrow BRDF

K.E Torrance and E.M. Sparrow developed an early BRDF model that aimed at capturing the off-specular reflectance as θ_r approaches 90° of rough surfaces where an off-specular peak existed [7]. The Torrance-Sparrow (T-S) model defines a surface roughness, σ_m, and treats this surface as individual micro-facets of area, A_f. The surface roughness must obey the fundamental geometrical optics assumption that the scale of roughness is larger than the wavelength of light that scatters from it. The T-S model then combines the specular reflection and diffuse reflection terms into a single model. Specular reflection is computed specific to each micro-facet and the surface normal angular positions, α, are distributed according to a Gaussian probability distribution function, $P(\alpha)$, by the Fresnel equations. The diffuse component is the result of multiple microfacet reflection or internal scattering.

The parameters required to produce the T-S BRDF predictions are the refractive index, $\tilde{n}$, to compute the specular Fresnel reflectance, and a roughness parameter, c, which defines

the distribution of facet slopes relative to the normal plane. This distribution was modeled as

$$P(\alpha) = be^{-c^2\alpha^2}, \tag{2.36}$$

where b is a scale factor. The surface roughness increases as c increases.

The major achievement of the T-S model was the introduction of a geometric attenuation factor, G, which incorporates shadowing and masking. Shadowing occurs when adjacent microfacets block incident energy while masking occurs when adjacent microfacets block specular reflections. The T-S BRDF model may be be written as

$$f_{TS} = \frac{F(\theta_i', \tilde{n})A_f G(\theta_{i,p}, \theta_{r,p})P(\alpha)}{4cos\theta_i cos\theta_r} + \frac{a}{d\omega_i} \tag{2.37}$$

where θ_i' is the angle of incidence relative to a local microfacet normal. The θ_{ip} and θ_{rp} angles relate the angle of incidence and angle of reflection to the surface and facet normals. The function F is the Fresnel reflectance for θ_i' for a material of complex index of refraction $\tilde{n}$. Volume scattering is given by the second term in the function and contains a constant, a, which represents the incident radiance that is scattered diffusely and $d\omega$ which is the reflected solid angle. The Torrance and Sparrow BRDF was able to capture off-specular reflectance peaks introduced by surface roughness.

2.3.2 Beard-Maxwell BRDF

The Beard-Maxwell BRDF was an extension of the generalized microfacet BRDF model approach to include polarized BRDF predictions [20]. Similarly to the Torrance-Sparrow model, the model separated the diffuse and specular contributions. A modified form of the Beard-Maxwell is commonly utilized today within the non-conventional exploitation factors database (NEF) [23] which contains material properties at the visible and infrared wavelength regions for a variety of man-made surfaces. The implentations of the Beard-

Maxwell BRDF within the NEF database is computed by

$$f_{BM}(\theta_i, \phi_i, \theta_r, \phi_r) = R(\beta, n, k)\frac{BRDF_{FS}(\theta_N)cos^2(\theta_N)}{R(0, n, k)cos(\theta_i)cos(\theta_r)}SO(\beta, \theta_N, \tau, \omega)+\rho_D+\frac{2\rho_v}{cos(\theta_I)+cos(\theta_R)}, \tag{2.38}$$

where the input parameters are listed in Table 2.1. The major achievement of the Beard-Maxwell model was an empirical function that derived the shadowing and obscuration parameters represented by

$$BRDF_{FS}(\theta_N) = \frac{R(0, n, k)B}{4cos^3(\theta_N)(\sigma^2 + tan^2(\theta_N)).} \tag{2.39}$$

The shadowing and obscuration function, SO is expressed in terms of those parameters and is dependent on the specular angle relative the normal of the the surface scattering element and the zenith angle of the scattering element relative to the material surface normal. The shadowing and obscuration function may be represented as

$$SO(\beta, \theta_N, \tau, \Omega) = \frac{1 + \frac{\theta_N}{\Omega}e^{-2\beta/\tau}}{1 + \frac{\theta_N}{\Omega}}. \tag{2.40}$$

The above SO function above is a simplified version that was implemented into the NEF database and the original Beard-Maxwell model also includes additional volume scattering parameters. The diffuse scattering term, ρ_D was included in the NEF modified version because this term demonstrated a better fit between model predictions and experimental measurements.

2.3.3 Priest-Germer BRDF

The Beard-Maxwell BRDF model was a polarized model in nature due to the inherently polarized Fresnel reflectance term. This concept was expanded upon in the Priest-Germer model by implementing a 4x4 element Mueller matrix for the Fresnel scattering factor [8]. The model predicts a polarized BRDF in the form

$$f_{PG}(\theta_i, \theta_r, \delta\phi) = \frac{1}{2\pi}\frac{1}{4\sigma^2}\frac{1}{cos^4\theta_N}\frac{e^{-(tan^2\theta_N/2\sigma^2)}}{co\theta_i cos\theta_r}M(\theta_i, \theta_r, \Delta\phi) \tag{2.41}$$

Table 2.1: Beard-Maxwell BRDF input parameters

variable	description
f_{BM}	total BRDF
$R(\beta, n, k)$	Fresnel reflection coefficient for angle β and index of refraction $n - ik$
β	specular angle relative to normal of surface scattering element
$BRDF_{FS}$	first surface BRDF based on experimental measurements
θ_N	zenith of scattering element relative to the material surface normal
θ_i	incident direction zenith angle
θ_r	reflected direction zenith angle
ϕ_i	incident direction azimuth angle
ϕ_r	reflected direction azimuth angle
SO	shadowing and obscuration function
ρ_D	diffuse scattering parameter
ρ_V	volumetric scattering parameter
$n - ik$	complex index of refraction of material
σ	mean square value of the total slope at a point on the surface
B	facet normal distribution BIAS parameter
Ω, τ	parameters for shadowing and obscuration model

where surface roughness is defined as σ, the angle between the microfacet normal and the macro surface normal is θ_N, and the Mueller matrix is given by M. The model is very simple and the only required input parameters to derive a polarized reflectance state are the complex index of refraction, $\tilde{n}$ and the slope variance σ of the materials roughness. The three BRDF models previously described provided the basis for microfacetized BRDF model development.

2.3.4 microDIRSIG BRDF

The three BRDF models previously described provided the basis for microfacetized BRDF model development. The microDIRSIG radiative transfer model was developed by research professor Michael Gartley at Rochester Institute of Technology as a rigorous ray tracing physics-based model that could predict the DHR (2.33) of an accurate geometric surface without the use of empirical measurement [25]. The model is initiated by "shooting" discrete bundles of incident energy at a virtual surface from a user defined incident direction and then utilizes conventional ray tracing techniques [21]. This virtual surface is typically constructed to micron or millimeter spatial resolution facets. Material characteristics are attributed by specifying the optical properties at the facet level. As a bundle of energy intersects a surface facet, the optical properties of that particular facet (namely bi-directional reflectance distribution and bi-directional transmission function) are queried and utilized to determine the intensity and direction(s) that the bundle will follow. At material interfaces, there may be any combination of reflected, transmitted, and absorbed light. A Jones Matrix ($2x2$) is used to describe all three events at every surface interaction and the bundle continues to bounce around surface facets until it leaves and intersects a hemispherical type virtual sensor that accrues its complex valued Jones Matrix value in the appropriate angular bin.

The model treats complex surfaces as microfacets and contaminants as geometrical objects which may be placed on the facetized surface [25]. All surfaces must be well de-

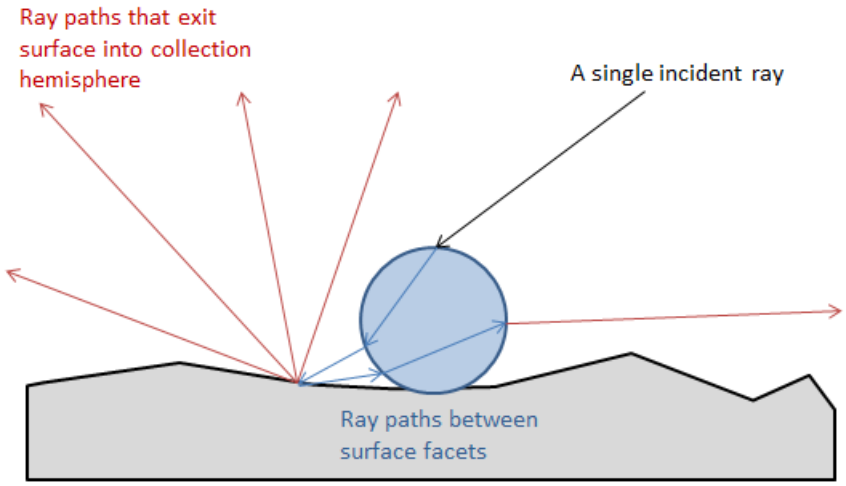

Figure 2.4: Illustration of possible ray paths for a simple facetized substrate surface with a single spherical liquid droplet. The red paths are recorded as reflected energy in their particular zenith/azimuth bin while the blue paths are intermediate paths between surface facets.

scribed by their optical constants. An illustration of a facetized rough surface with a single spherical liquid droplet is presented in Figure 2.4. The possible ray paths are color coded to represent the incident ray (black), intermediate rays between surface facets (blue), and rays leaving the surface (red) into the above hemisphere.

The resulting output for a microDIRSIG simulation is a hemispherical projection of collected wave power in terms of a 4x4 Mueller Matrix. Each simulation occurs at a single wavelength and ray propagation is unique to each specified wavelength in order to ensure accurate modeling. Radiometric quantities such as BRDF and emissivity may be derived from the model outputs with appropriate processing. A single microDIRSIG simulation of silica sand at 10 microns is presented below in Figure 2.5. The image is a hemispherical projection of the reflected directions in zenith and azimuth angle space over the entire two pi steradians above the surface. Here the first columm of the Mueller Matrix is displayed

for a 45 degree off-nadir angle of incident energy. In order to extract spectral reflectance, the simulation must incrementally step through the spectral range returning the integrated BRDF (DHR) at each respective wavelength.

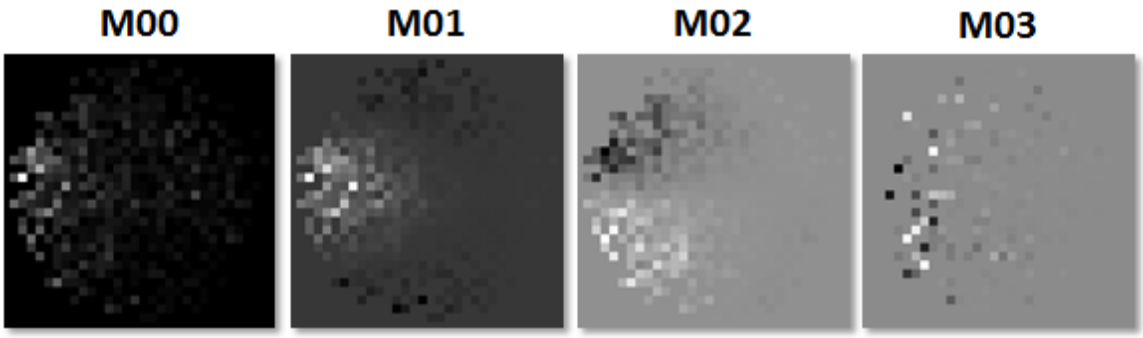

Figure 2.5: microDIRSIG modeled BRDF of silica sand at 10.00 microns, showing the first column elements of the 4x4 Mueller matrix. The M00 reflectance corresponds to total, unpolarized reflectance, while the M01 corresponds to horizontal (brighter) and vertical (darker) polarization and the M02 and M03 correspond to +/-45 degree linear polarization and circular polarization states respectively. Gray level indicates relative reflectance.

2.4 Radiometry and Radiation Propagation

To quantitatively analyze the electromagnetic radiation propagating through the atmosphere, passive remote sensing systems that encompass the 0.4 to 15 μm spectral region were developed. The passive spectral region can be divided into two sub regions based on where the measured radiation originates [1]. Radiation originating from the sun is referred to as solar radiation and pertains to the visible (VIS), near infrared (NIR), and shortwave infrared regions (0.4 to 2.5 um) while radiation emitted from objects is referred to as thermal radiation and pertains to the longwave (LWIR) region (8 to 15 um). Remote sensing in the MWIR region (3 to 5 um) includes contributions from both the solar and

thermal regions.

2.4.1 Radiometry

Radiometery is a field in science that characterizes how much electromagnetic radiation is present at a specific time, location, or direction in space [1]. Light travels in straight lines and transfers energy in a measurable quanta. The energy carrier of light is called a photon and is expressed as

$$q = hv = \frac{hc}{\lambda}, \tag{2.42}$$

where energy, q is represented in Joules [J]. The constant h is equal to $6.6256 \cdot 10^{-34} [Joules \cdot sec]$ and refers to Planck's constant which describes the proportionality between the energy and the frequency, v of the electromagnetic wave. From this relationship, we see that wavelength is inversely proportional to frequency and shorter wavelength light carries more energy than longer wavelength light. The total energy can then be thought of as the sum of energy over all frequencies.

$$Q = \sum_{i=1} q_i = \sum_{i=1} n_i h v_i \tag{2.43}$$

Power is often thought of as a rate at which energy is propagating and can be quantified as the first time derivative of the total radiant energy Q. A sensor measures irradiance, which is the radiant flux delivered to the surface area of the detector and can be defined as

$$E = E(x, y) = \frac{d\Phi}{dA} [W m^{-2}], \tag{2.44}$$

where Φ represents the power and dA represents the area of the detector. Irradiance, however, only provides the spatial information about the incident power, and can vary based on the angular orientation of the sensor relative to the scene geometry. Therefore, the solid angle, $d\Omega$ is introduced which is defined as the conic angle encompassing the

detector area dA. The solid angle is represented by $d\Omega = dA/r^2[steradian]$ where r is the distance from the source to the projected area. This allows us to define radiance, L as the flux incident upon the detector area with angular dependence. Radiance is defined as

$$L = L(x, y, \theta, \phi) = \frac{d^2\Phi}{dAcos\theta d\Omega} = \frac{dE}{d\Omega cos\theta} \tag{2.45}$$

where now θ and ϕ define the angular components of the flux normal to the x, y plane.

2.4.2 Blackbody Radiators

The term blackbody was first formulated by Gustav Kirchoff in the 19th century to describe an idealized object that perfectly absorbs all incident radiation and then re-radiates it [9]. Natural blackbody materials do not exist, however they can be experimentally set up by having a cavity with a small aperture that causes incident light to enter and bounce around several times before exiting, thus capturing all photons. Max Planck, in 1901 derived an expression to describe the spectral radiant exitance of the blackbody. This derivation led to Planck's law which can be written as

$$M_\lambda = 2\pi hc^2\lambda^{-5}(e^{\frac{hc}{\lambda kT}} - 1)^{-1}[Wm^{-2}\mu m^{-1}] \tag{2.46}$$

where T is the temperature in degrees Kelvin, k represents the Boltzmann gas constant ($1.38 \cdot 10^{-23} jK^{-1}$), and h and c are the previously defined Planck's constant and speed of light respectively. Radiant exitance is a function of wavelength and temperature and Figure 2.6 displays an example spectral exitance curves when held at a constant temperature. In the LWIR region, it is clearly evident that objects around the average temperature of Earth's surface (287 K) have a measurable spectral exitance.

Blackbody materials do not exist on Earth's surface and therefore the concept of emissivity $\epsilon(\lambda)$ is introduced. Emissivity is spectral quantity that represents the fraction of spectral exitance $M_\lambda(T)$ radiating from an object at a temperature, T compared to the

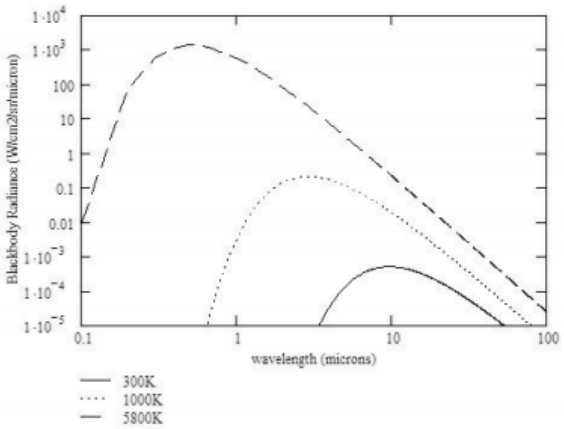

Figure 2.6: Spectral exitance of blackbodies at different temperatures [5]

exitance that a blackbody would emit at that same temperature $M_{\lambda BB}(T)$, i.e.,

$$\epsilon(\lambda) = \frac{M_\lambda(T)}{M_{\lambda BB}(T)} \tag{2.47}$$

Emissivity is a fundamental form of matter similarly to reflectivity (ρ), absorptivity (α), and transmissivity (τ). Kirchoff's law states that for objects in thermodynamic equilibrium, emissivity is numerically equal to the absorption and the conservation of energy law can be rewritten as

$$\epsilon + \tau + \rho = 1. \tag{2.48}$$

For opaque objects, the transmission term is zero and

$$\epsilon + r = 1. \tag{2.49}$$

2.4.3 Thermal Radiation Paths

When working in the LWIR region of the spectrum, all of the solar radiation terms are negligible. The sensor reaching radiance is comprised of the direct thermal radiation from the target, the downwelled radiance caused from atmospheric emission that is reflected

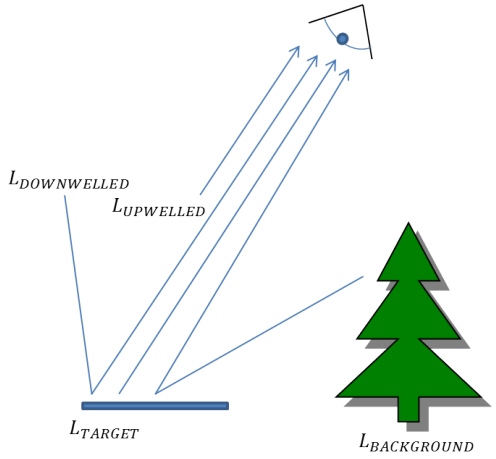

Figure 2.7: Possible paths a photon can take in the LWIR before reaching a detector

off the target, reflected thermal radiation from background objects, and the direct atmospheric radiation or skylight captured by the sensor. The different photon pathways are illustrated in Figure 2.7. At-sensor reaching radiance is simply a summation of all the contributions and in a generic sense can be written as

$$L_{SENSOR} = L_{TARGET} + L_{BACKGROUND} + L_{DOWNWELLED} + L_{UPWELLED} \quad (2.50)$$

Computing the contributions from each of these terms is important for deriving the targets surface properties. The governing equation was developed for approximating the contributions from each term, allowing for extraction of the surface parameters.

2.4.4 Governing Equation

We have now covered how photons are emitted in the infrared from a source and how they propagate through the atmosphere to the sensor. We also discussed all the different photon pathways that comprise the aperture reaching radiance measured by a sensor. Remote sensing analysts are generally concerned with the surface properties pertaining to

the direct photon pathway from the target to the sensor. All other parameters involved in the measured radiance contribute a finite radiance which must be accurately estimated in order to extract the surface parameter of interest. The governing equation was developed in order to characterize atmospheric parameters and to estimate the abundance of radiance measured from the other photon pathways.

The governing equation in the thermal infrared assuming a uniformly reflective Lambertian surface for simplicity can be expanded to

$$L(\lambda) = \left[\epsilon(\lambda)L_{T\lambda} + (FE_{d\lambda} + (1-F)E_{b\lambda})\frac{r_{d\lambda}}{\pi}\right]\tau(\lambda) + L_{u\lambda} \tag{2.51}$$

where the four terms correspond to the four thermal paths previously defined. The first term $\epsilon(\lambda)L_{T\lambda}$, which represents the direct thermal radiation emitted from the target L_{TARGET}, is often the most dominant term and contains the spectral emissivity. Typically, emissivity of the target is the parameter of interest in the LWIR. Deriving emissivity however, poses an underdetermined problem in the sense that there are always N equations, and $N+1$ unknowns where N corresponds to the spectral dimension of the data and the additional unknown quantity is the temperature of the surface. There are several methods for estimating the temperature and this topic is further explained in chapter 4.

2.5 Chapter Summary

This chapter began by providing a historic overview of how electromagnetic radiation has been described. The Fresnel equations and Mueller matrix calculus were introduced as a way to describe the properties of electromagnetic radiation. The optical scatter of electromagnetic radiation off surfaces was then described by introducing physics based bidirectional reflectance distribution models. Several BRDF models were discussed leading up to the development of the microDIRSIG radiative transfer model. The overall objective of the upcoming chapters is providing empirical measurements for the validation of the microDIRSIG model.

Next, infrared radiometry was introduced by discussing the early developments of Planck's law for blackbody radiation and the concept of Kirchoff's law for extracting spectral emissivity. Understanding how electromagnetic radiation originates and the different pathways it may take in the LWIR is important for extracting useful information from a sensor. The governing equation was introduced as a method for approximating the radiance contributions from non target sources which is necessary for extracting the surface parameters utilized for microDIRSIG comparison.

Chapter 3

Prior Work and Recent Advances

Verification and validation are important steps that are completed during the development of all types of simulation models in an attempt to prove the credentials of the model. Verification is defined as the substantiation that a computerized model represents the conceptual model within specified limits of accuracy or that the model is operating as intended [22]. Validation can be defined as the substantiation that a computerized model within its domain of applicability possesses a satisfactory range of accuracy consistent with the intended application of the model. As touched upon earlier, several BRDF models exist, and verification and validation typically rely on empirical measurement.

This chapter is broken up into two parts. The first section covers past experiments designed to measure the spectral effects of contaminants on surfaces with infrared spectrometers. Reliable measurements and appropriate data processing are important considerations when validating a model. A high level of ground truth data is required to best represent real-world situations within the modeling environment. The second section covers past model validation techniques including previous experiments designed toward microDIRSIG validation. These techniques involve comparing predicted emissivity of liquid contaminated surfaces against an analytical thin film model and infrared interferometer measurements.

3.1 Measuring Contaminated Infrared Spectra

Several past research efforts examined the BRDF and measurement validation of pristine surfaces that are only present in laboratory settings. Often in real world scenarios, natural materials almost always contain contamination. The following subsections present recent work completed in extracting the optical properties of contaminated surfaces and how varying amounts of a contaminant may affect the spectra.

3.1.1 Natural Contaminants

In 2006, Strackerjan et al. [11] executed several field and laboratory measurements of surfaces with the natural environmental contaminants of soil and water. The purpose of this experiment was to replicate more realistic scenarios and provide spectra that capture the variability that may arise from outdoor natural settings which could lead to extended simulation capability. The experiment was carried out over the visible spectrum (400 to 2500 nm) by utilizing an Analytical Spectral Devices (ASD) FieldSpec Pro and the LWIR spectrum (8 to 14 μm) by using a Design and Prototypes Instruments 102F FTIR Spectrometer.

The field measurements were executed on a series of vehicles (blue Ford, green Subaru, and a white Saturn) in four different contaminant conditions: 1. dirty and dry, 2. dirty and wet, 3. clean and wet, and 4. clean and dry. The instruments rested on a tripod and were placed on a scaffold above the car at a nadir viewing angle on the opposite side of the sun to minimize shadowing or adjacency contributions from the scaffold. Results of the field measurements showed similar trends for all vehicles. The surface reflectance decreased with the presence of water and increased due to the effect of road dust, although less significantly. In the LWIR, the emissivity increased with the presence of water and decreased due to the effect of road dust. These results showed that the application of natural contamination can have a significant effect on the measured optical properties of the

material, however limitations arise when trying to quantify the amount of contamination.

The laboratory measurements were completed to control the amount of contaminant applied. Asphalt, concrete, red painted metal, and a roofing shingle were all measured with varying coverage of sand. Additional measurements of asphalt and concrete were taken with water as the contaminant. For the ASD reflectance measurements, an artificial light source was used to illuminate the samples. The ASD is designed such that a fiber optic bundle transmits light from the input optic to the detector and subsets of these bundles correspond to different wavelengths. The design may cause discontinuities within the spectrum for heterogeneous surfaces due to the different detectors observing different areas. A potter's wheel was used to rotate the sample during the collect and the spectra was temporally averaged. Because of this setup, the water was difficult to measure for smooth surfaces and was neglected for the metal and roofing shingle sample. The thermal radiance measurement also required a unique laboratory setup due to the necessity of thermal contrast between the material surface and the background irradiance. To accommodate for this, an artificial cold sky was created by suspending ice filled, uniformly black painted bins above the sample. The samples were also heated to create as much separation as possible for the emissivity retrieval.

Results for the laboratory measurements generally showed a gradual transition from the spectra of the pure sample to the spectra of sand, however some non linearity in the reflectance as a function of area sand coverage did arise for the red painted metal and sand sample. All of the emissivity measurements showed a consistent linear trend as the sand coverage increased. For the water samples, it was observed that only a very small amount of water significantly decreased (increased) the reflectance (emissivity). There was non linearity in both samples with relation to area coverage. The emissivity spectra also experienced an unknown decrease in emissivity after 11.5 microns. Explanation for this phenomenon was speculated to be radiative cooling and evaporation processes that contributed to an increase in moisture which led to transmission and path radiance changes.

The research did show that natural contaminants can considerably alter the reflective or emissive spectra obtained from real world scenarios.

3.1.2 Liquid-Contaminated Surfaces

There has been high desire for standoff detection and classification of chemicals on surfaces for many civilian and military applications. Long wave infrared spectroscopy has demonstrated to be a promising technique for standoff detection on pristine surfaces [12]-[14].

In 2011, Goyal et al. [15] investigated infrared signature phenomenology of the liquid chemical, diethyl phthalate (DEP) on realistic natural surfaces such as concrete pavers, weathered asphalt, and sand. Calibrated reflectance measurements in the LWIR were performed with varying controlled levels of DEP applied to the surfaces. The results for each surface (Figure 3.1) did vary based on the surface characteristics. Weathered asphalt, which is a coarse composite of minerals and generally non-porous in nature showed the most prominent spectral features of DEP (local spectral minimum at 9.28 and 9.6 microns) and the largest ratio minimum depths. Concrete, a composite of water, aggregate, and cement seemed to readily absorb the contaminant and therefore had similar features that were much less defined in the reflectance spectra but still fairly significant in the reflectance ratio plots. Finally, the sand sample, which is highly porous in nature, showed an overall decrease in spectral reflectance but much lower reflectance ratio depths. The results demonstrated that infrared spectroscopy had reasonable potential for classifying liquid contaminants on surfaces.

A common application of liquid-contaminant detection is the identification of hazardous substances. It is often difficult to take experimental measurements because the preparation of samples can be dangerous or not possible. Therefore, radiative transfer modeling can provide a useful tool for predicting liquid contaminated spectra which could lead to improved methods for automatic remote detection and identification.

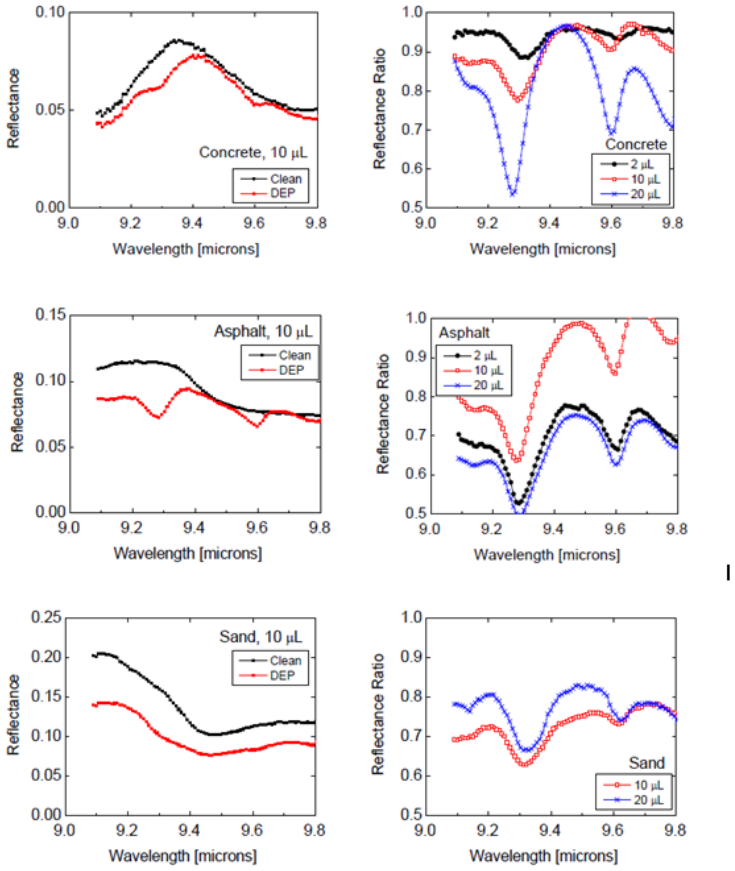

Figure 3.1: Reflectance and reflectance ratio for for clean and DEP contaminated samples of concrete (top), asphalt (middle), and sand (bottom). [15]

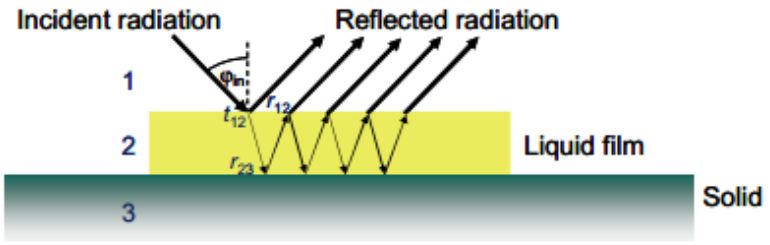

Figure 3.2: Reflected radiation for a liquid film on a solid surface [16]

3.2 Previous Model Validation Techniques

In 2008, Harig et al. [16] developed a radiative transfer model that takes into account the complex index of refraction to predict the reflectance of a liquid-contaminate surfaces. The liquid and background surfaces are modeled as planar homogeneous absorbing dielectric materials and all reflections are assumed to be specular. Therefore the reflection coefficients (r_{12} and r_{23}) can be computed by using the Fresnel equations (Figure 3.2). This computation requires knowledge of the complex index of refraction or the linear absorption coefficient of the liquid.

The radiative transfer model was validated by comparing model predicted spectra and measured spectra obtained by using an imaging Fourier transform spectrometer (IFTS) that was developed at the Hamburg University of Technology. Background materials consisted of clay, wood, and steel and the contaminate used was methyl salicylate. The samples were actively illuminated by an infrared source and the experiment was set up as Figure 3.3.

Spectra were compared in brightness temperature units and the model predicted spectra showed an excellent agreement to the measured data. The model however has several limitations [16]. The primary limitation is the need of a planar surface and the absence of a diffuse reflection term. Most natural surfaces contain a degree of roughness

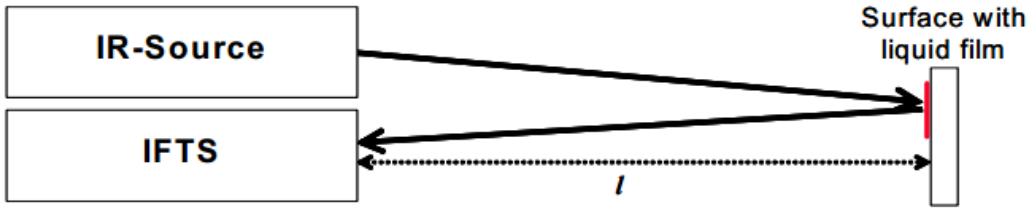

Figure 3.3: Experimental measurement setup used for radiative transfer model validation. [16]

which will change the direction of specular reflection and volumetric scattering leading to scattering in all directions above the sample. The measurements were also performed using an active source of illumination which limits the range of possible detection. A passive source would allow for a more standoff detection, however an effective method for estimating the downwelled sky radiance would need to be incorporated into the model. This work did show that the reflectance of liquid contaminated surfaces can be estimated by radiative transfer modeling.

3.2.1 microDIRSIG Validation

The microDIRSIG model extends on the functionality of the other microfacetized BRDF models mentioned in chapter 2.3 by allowing surface contaminants to be placed in a scene as well defined geometric objects. Initial model validation was completed by comparison between an analytical thin film model that utilizes the Transfer Matrix Method (TMM) [17]. The TMM model is commonly used in the optics community for predicting reflectance, transmission, and emissivity spectra of thin film liquids on substrates. An optically smooth aluminum sample with a thin film of SF96 silicone oil was modeled in microDIRSIG and compared against the analytical thin film model at three film thicknesses [18]. The film thicknesses corresponded to 0.25, 0.50, and 1.25 microns and the angle of incidence was set to 45 degrees. Results showed a very promising agreement

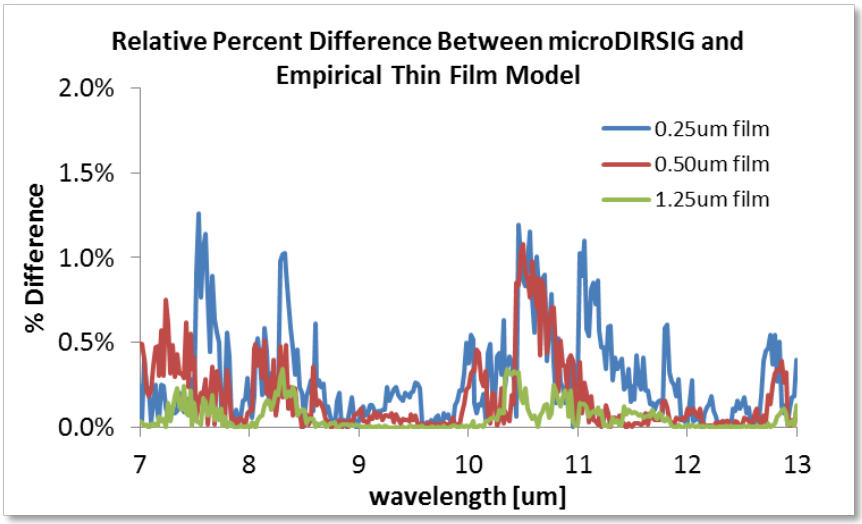

Figure 3.4: Absolute percent difference in modeled emissivity between microDIRSIG and analytical thin film model. [18]

(Figure 3.4) with maximum percent differences around 1%. The TMM model weaknesses are that it assumes a spatially homogeneous surface with an infinitly extending thin film layer and is therefore limited in the surfaces that can be modeled.

A collection of empirical experiments were also completed to further validate the microDIRSIG model for well defined surfaces. One such experiment was a simple 100% silica sand in two different grain distributions, and a SF96 silicone oil contaminated version of the two sand types [19]. The different samples (small and large grain) ranged in size from 425-1000 microns and 1000-1400 microns. The contaminant was applied by mixing with 0.3% (by weight) of SF96 to each grain size. Samples were formed as thin layers in shallow containers and measured with a Design and Prototypes FTIR spectrometer from nadir and 45 degree off-nadir viewing angles.

Sand geometries were constructed in a computer aided design program (Figure 3.5) and surfaces were attributed with a spectral complex index of refraction taken from [29]. The SF96 was applied within the model as a film thickness on the sand particles which

was calculated by determined the thickness required to achieve the dosing level of 0.3%. Optical properties of SF96 were also taken from literature [32] and input into the model. The model output was a bidirectional hemispherical reflectance spectral cube. Directional hemispherical emissivity was derived by integrating over each spectral cube.

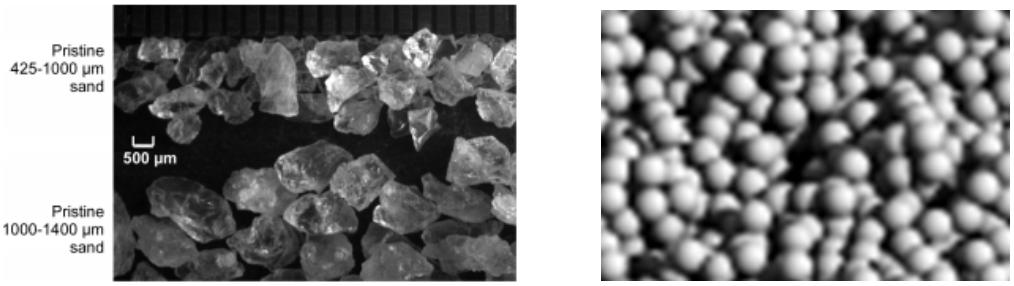

(a) (b)

Figure 3.5: Microscope images of silica sand (a) and virtual sand generated for model validation (b) [19]

Results showed a clear and consistent trend of higher emissivity values with the addition of SF96 for both grain sizes (Figure 3.6) in the Restrahlen bands between 8 and 9 microns [19]. Additionally, the measurements showed a greater difference between the emissivity of the plain sand with respect to the grain size. The model made a few assumptions that may have led to the discrepancies between the spectra. First, the sand was modeled as spherical particles instead of random irregular shapes observed in real sand. Also, the sand was considered homogeneous within the model as opposed to the natural heterogeneous nature the measured sand was. The presence of the contaminate however was easily distinguishable in both the modeled and measured outputs.

3.3 Chapter Summary

This chapter assesses the current modeling and measuring capabilities of contaminated surfaces. The first half focused on a few previous experiments aimed toward identifying how the presence of contaminates affected the optical properties of surfaces. Results of this prior experimentation have suggested that contamination is an important consideration and may affect the performance of material identification and target detection algorithms.

The second section of this chapter introduced previous techniques in validating radiative transfer models. The microDIRSIG model is a unique model that builds upon the microfacetized modeling blueprint and allows for contaminants to be placed on micron resolution surfaces. These increased modeling capabilities can potentially lead to increased performance for standoff detection of contamination for many important applications. Two previous microDIRSIG validation techniques including comparisons to an analytical model and comparisons to contaminated sand measurements were described. There is desire for an extension of the previous validation techniques to include more microDIRSIG and measurement comparisons.

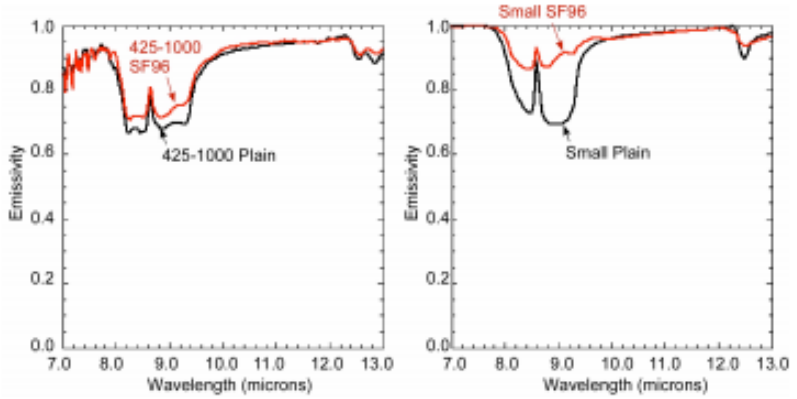

(a)

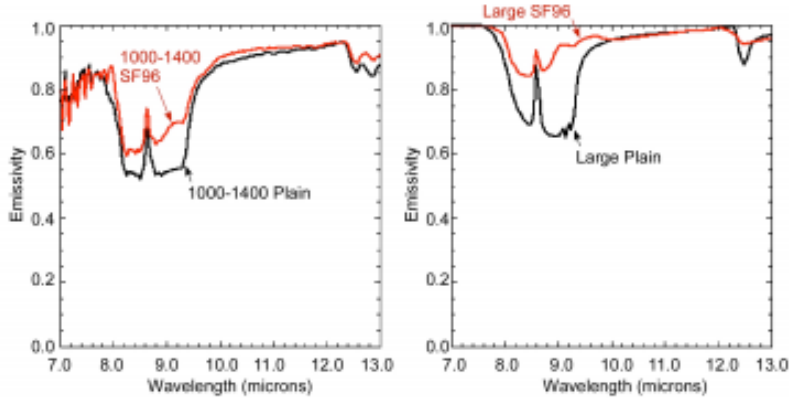

(b)

Figure 3.6: Comparison of empirical (left) and model predicted (right) spectral emissivity with and without SF96 for small (a) and large (b) grain silica sand [19]

Chapter 4

Empirical Measurement

This chapter gives a detailed overview of the experiments that were executed for the microDIRSIG model validation. Section 4.1 provides a description of the experiment completed at Physical Sciences Inc headquarters. The following sections provide a description of the instruments used for obtaining the measurements and the data processing steps. Emissivity was the fundamental output of the microDIRSIG model and therefore, the emissivity spectra and the methodology for extracting it is presented here for each instrument. Section 4.4 then describes additional measurements that were taken at RIT for further model validation.

4.1 Andover Experimental Setup

On July 17th, 2014, RIT and PSI executed a joint data collect at PSI headquarters in Andover, Massachusetts. The purpose of the experiment was to collect LWIR radiance spectra over a variety of modalities for microDIRSIG model validation. Samples that had a mature characterization history such as wood (WO) and polished aluminum (AL) were measured with varying contamination levels of SF96 (polydimethylsiloxane) oil applied by a spray bottle. A total of nine aluminum and nine wood plates were prepared with different

paint finishes and different contamination levels. The paint finishes consisted of no paint (Bare), Krylon ultra-flat black (UFB), and Krylon glossy black (GB). The contamination levels (CL0, CL1, CL2, and CL3) corresponded to clean, $25\frac{\mu g}{cm^2}, 50\frac{\mu g}{cm^2}, and 100\frac{\mu g}{cm^2}$ respectively. Originally, we planned for contamination levels to be the CL2 and CL3 amounts for all samples; however CL2 seemed to completely saturate the surface of the aluminum and rested as a thin layer. The second contamination level for aluminum was changed from CL3 to the CL1 amount because it was believed $100\frac{\mu g}{cm^2}$ SF96 on aluminum would be too thick of a contaminant layer and may run off the sample.

The samples are shown in Figure 4.1 and labeled in the corresponding tables. Each sample was measured by a Design and Prototypes (D&P) model 102 FTIR spectrometer, and PSIs AIRIS instrument. Figure 4.2 shows the typical sky conditions during the data collect.

(a)

(b)

UFB Al - Clean	UFB Al - CL2	UFB Al - CL1
GB Al - Clean	GB Al - CL2	GB Al - CL1
Bare Al - Clean	Bare Al - CL2	Bare Al - CL1

(c)

UFB Wo - Clean	UFB Wo- CL2	UFB Wo - CL3
GB Wo - Clean	GB Wo - CL2	GB Wo - CL3
Bare Wo - Clean	Bare Wo - CL2	Bare Wo - CL3

(d)

Figure 4.1: Target layout for Andover measurements. (a) Photo of prepared Aluminum (12 x 12 inch) samples; (b) Photo of prepared Wood (8 x 8 inch) samples; (c) Table labeling the aluminum samples; (d) Table labeling the wood samples.

Figure 4.2: Sky conditions for Andover measurements.

4.2 Design and Prototypes Model 102 FTIR Spectrometer

The model 102 FTIR spectrometer developed by Designs and Prototypes is a Fourier transform infrared spectrometer that contains a miniature Michelson interferometer with input optics, an infrared detector, drive and sampling electronics, and an embedded PC type computer. The system is bundled into a small portable case that is ruggedized and sealed from the environment, allowing for use in any field condition. Light passes through the fore optic through an aperture and lens and enters the interferometer where internal mirrors are servo driven at a constant speed, producing interference patterns. Output light is then focused on a liguid nitrogen cooled detector, having a spectral range of 2 to 16 microns. The spectral resolution is 4 wavenumbers and the wavelength is calibrated by a temperature controlled laser diode that serves as a reference for the servo and sampling electronics [26].

The detachable fore optic rotates and contains an eyepiece allowing the user to aim the

fore optic at the target of interest. This fore optic is approximately 1 inch in diameter with a 4.8 degree field of view, giving a sample spot size of about 3 inches when used from nadir 3 feet above the sample. The instrument is meant for close range sensing and typically rests on a tripod. The PC runs Windows 2000 and contains software that enables the user to accumulate real time radiance data to allow post-processing retrieval of emissivity spectra. Each emissivity computation requires four radiance measurements that include a cold and warm blackbody, the sample measurement, and the downwelling radiance using a highly reflective infragold plate.

The D&P model 102 was used to measure each sample separately. A digital in-

Parameter	Value
Spectral Range	2 – 16 microns
Spectral Resolution (FWHM)	4 cm^{-1}
Size (WxDxH)	36x20x23 cm
Weight	< 7 kg

Figure 4.3: D&P model 102 FTIR spectrometer and instrument parameters. [26]

clinometer was used to set the foreoptic at a 45 degree off-nadir viewing angle for the Andover measurements. An electronic blackbody with an adjustable temperature is sup-

plied with the instrument and the cold and warm temperatures were set to $10°C$ and $60°C$ to bracket the range of temperatures for all samples. The choice of a low cold blackbody temperature allows for a more accurate calibration of the downwelling radiance, because the apparent temperature of the sky is typically much lower than the samples. The hot blackbody should be set at a temperature just above the highest sample temperature. There is typically a trade-off between obtaining a more accurate sample calibration and a more accurate downwelling calibration depending on how different the low blackbody temperature is from the sample and the sky. The calibration process is further explained in the following section.

4.2.1 Calibration

Calibration is a crucial data processing step and the hot and cold blackbody measurements provide a standard for relating the raw instrument spectra to an analytically computed radiance spectra obtained from Planck's equation. Blackbody measurements and calibration are required frequently because all thermal instruments tend to have natural thermal drift that may be difficult to characterize. An extra data processing step was incorporated into the calibration to account for this and is further explained in 4.2.1. The calibration procedure assumes the blackbody's emissivity is unity and that the instruments response to incoming flux is linear over the range of interest [27]. Calibrated spectral radiance is obtained by computing the spectral responsivity and an intercept which represents the offset. The responsivity $R(\lambda)$ is computed by

$$R(\lambda) = \frac{V_H(\lambda) - V_L(\lambda)}{L_{BB}(T_H, \lambda) - L_{BB}(T_L, \lambda)} \tag{4.1}$$

where $V_H(\lambda)$ and $V_L(\lambda)$ are the uncalibrated magnitude measurements of the warm and cold blackbodies respectively and the terms $L_{BB}(T_H, \lambda)$ and $L_{BB}(T_L, \lambda)$ represent the spectral blackbody radiance at the respective hot and cold temperature using Planck's

function 2.46. The offset $L_0(T_{inst}, \lambda)$ is then computed by

$$L_0(T_{inst}, \lambda) = L_{BB}(T_L, \lambda) - \frac{V_L(\lambda)}{R(\lambda)}. \tag{4.2}$$

Given the responsivity and the offset, the conversion from uncalibrated instrument counts to calibrated spectral radiance is given by

$$L(\lambda) = \frac{V(\lambda)}{R(\lambda)} + L_0(T_{inst}, \lambda) \tag{4.3}$$

where the units are $W/cm^2/sr/\mu m$.

Effect of Thermal Drift

Frequent calibration is required because of thermal drift associated within the instrument. This occurs due to temperature change happening in the field during the course of measurements. If the instrument experiences thermal drift after calibration, error is propagated through the calibration and data processing. Figure 4.4 shows the raw instrument counts measured from cold and warm blackbodies manually set at 10° and 60° at a range of different times that cover a two hour period during the Andover data collect. The black curve represents an interpolated calibration curve at a time of 11:11 am.

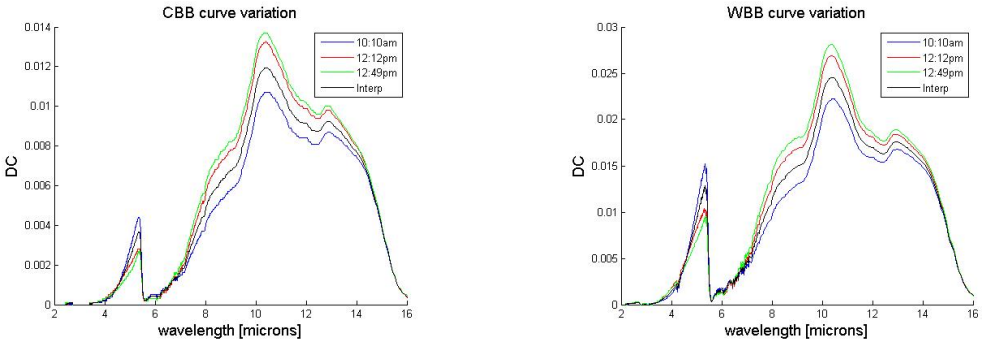

(a) Cold BB (b) Warm BB

Figure 4.4: D&P model 102 FTIR Thermal Drift

To compensate for this, the thermal drift was assumed to be linear and a time interpolation was performed to create pseudo calibration curves for each measurement. These new blackbody curves were then used to perform the calibration. The accuracy of this assumption was tested by interpolating blackbody curves at a time when measured blackbody curves were available for truth. Errors over the LWIR spectral range for the blackbody interpolation were very minimal as shown in figure 4.5. Figure 4.6 shows an example of how the interpolation adjusted the emissivity.

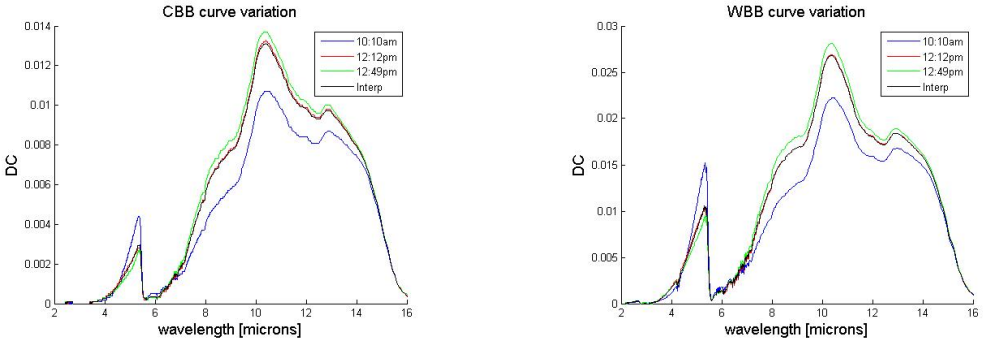

(a) (b)

Figure 4.5: D&P model 102 FTIR Thermal Drift Error for cold (a) and warm (b) blackbodies; Interpolated time was 12:12 pm

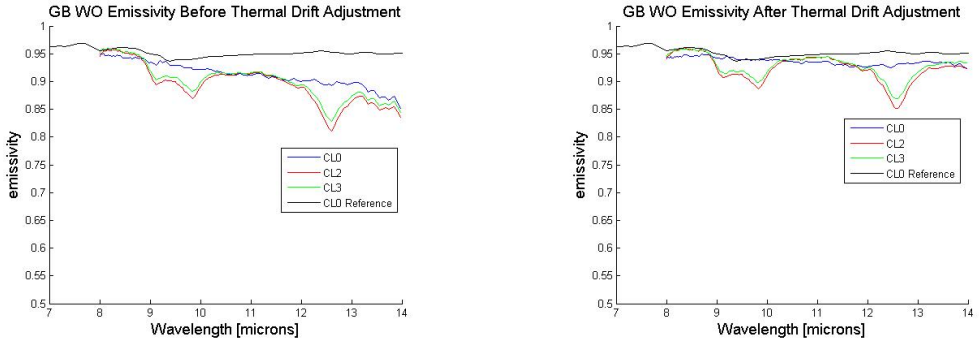

(a) (b)

Figure 4.6: Glossy Black Wood sample measurements for all SF96 contamination levels before (a) and after (b) blackbody interpolation and comparison to the Nonconventional Exploitation Factors Data System (NEFDS) for clean sample.

4.2.2 Downwelled Radiance

The atmosphere above the target also has a nonzero temperature and therefore radiates and scatters self-emitted energy onto the target. Some of this energy is then reflected up to the sensor and contributes to the measured sample radiance. The downwelled radiance field consists of many different terms because photons are released from all portions of the above hemisphere. Downwelled radiance can be numerically simplified by integrating all those terms over the hemisphere. The governing equation is simplified to

$$L(h,\theta,\lambda) = \tau(h,\theta,\lambda)[\epsilon(\theta_t,\lambda)L_{BB}(T_s,\lambda) + (1-\epsilon(\theta_t,\lambda))L_{DWR}(\lambda)] + L_{UWR}(h,\theta,\lambda) \quad (4.4)$$

where $L_{DWR}(\lambda)$ is the integrated downwelling radiance over the hemisphere representing the scattered, self-emitting, and direct solar contributions and $L_{UWR}(h,\theta,\lambda)$ is the upwelling scattered and self-emitted atmospheric path radiance reaching the sensor. Notice that each parameter is a function of the sensor height, h and angle, θ relative to the normal of the target.

This value can be measured by taking a sample measurement of a perfectly diffuse reflector. A diffuse infragold with an emissivity of 0.02 is provided with the model 102

package to approximate the downwelling radiance. This approach requires that the temperature and spectral nature of the plate are well known. The plate must also be placed in the same position as the target and downwelling measurements should be taken as close to the time of the sample as possible to correctly characterize the atmosphere.

4.2.3 TES Processing and Results

As mentioned before, computing the surface emissivity is a difficult task because the equation (2.51) is an under-determined problem if the temperature of the sample is unknown and the measured radiance consists of contributions from other radiant sources in the atmosphere. In order to solve for emissivity, the atmospheric transmission, downwelled radiance, and path radiance must be accurately estimated. The model 102 conducts measurements very close to the target, mitigating the effects of the atmosphere. Therefore, the atmospheric transmission and path radiance can be assumed to be 1 and 0 respectively. This assumption simplifies the governing equation to

$$L(h,\theta,\lambda) = \epsilon(\theta_t,\lambda)L_{BB}(T_s,\lambda) + (1-\epsilon(\theta_t,\lambda))L_{DWR}(\lambda) \tag{4.5}$$

where upon rearranging, the emissivity can be simply derived by

$$\epsilon(\theta_t,\lambda) = \frac{L(h,\theta,\lambda) - L_{DWR}(\lambda)}{L_{BB}(T_s,\lambda) - L_{DWR}(\lambda)}. \tag{4.6}$$

Here the calibrated radiance measured from the sample is $L(h,\theta,\lambda)$ and the calibrated downwelling radiance measured from the infragold is L_{DWR}. If the temperature, T_s of the sample is known, then the blackbody radiance term $L_{BB}(T_s,\lambda)$ can be computed via Planck's function and emissivity is easily obtained. For the Andover measurements, each sample temperature was measured using an Exergen Precision Infrared Handheld Thermometer, which uses a detector housed inside a hemispherical reflector. When in contact with a surface, all surface leaving radiance is multiply reflected between the hemispherical reflector and the target surface until reaching the detector thus driving the surface emissivity to unity.

If the temperature of the sample is unknown, there are several techniques that can be used to estimate the sample temperature. Horton et al., 1998, had proposed an iterative spectral smoothness method. The retrieved target temperature is found by selecting a small spectral range and iteratively computing the emissivity while stepping though sample temperature increments and holding the downwelling parameters constant [28][29]. A second order polynomial is fit through the defined spectral range and residual error are computed between the derived target emissivity and the computed second order polynomial. The retrieved temperature of the sample is the temperature that minimizes the residual error. This algorithm was performed using IDL codes provided by RIT Professor Carl Salvaggio. A spectral range of 10.5 to 11.0 microns was chosen and the measured and retrieved temperatures for all samples are listed in Table 4.1.

The retrieved temperature did differ from the measured temperature in some cases by up to 6 degrees Kelvin with one outlier for the highly reflective clean bare aluminum case. The thermometer does require to be placed in physical contact with the sample. In most cases, the sample contained a thin film of SF96 on the surface that may have caused temperature inaccuracies. Also, fluctuations in the surface temperature may have arisen due to effects of a breeze on the surface. Each sample was moved between instruments and potentially not given enough resting time to reach a thermodynamic equilibrium with the environment before each measurement. We also noticed fluctuations in sample temperature throughout the day as the sun illumination varied. The retrieved temperature seemed to consistently show improved emissivity results.

The emissivity spectra derived for each sample did show consistent results and the SF96 spectra did contain distinguishable spectral differences between the clean and contaminated samples. Figures 4.7-4.9 show derived emissivity for each contamination and paint combination for the D&P model 102 measurements. Each set of measurements did consistently show a distinct w shaped dip between 9 and 10 microns and a second dip between 12 and 13 microns when SF96 was present. The aluminum samples seemed to

Table 4.1: Sample Temperature Measurements and Temperatures Retrieved by TES

Sample	Sample Temp. (K)	Retrieved Temp. (K)	Difference (K)
Bare Al - Clean	311.6	343.3	31.7
Bare Al - CL1	312.9	311.6	1.3
Bare Al - CL2	312.3	314.7	2.4
GB Al - Clean	317.5	317.1	0.4
GB Al - CL1	317.0	322.2	5.2
GB Al - CL2	317.5	320.2	2.7
UFB Al - Clean	321.4	320.0	1.4
UFB Al - CL1	320.4	323.1	2.7
UFB Al - CL2	320.0	324.9	4.9
Bare Wo - Clean	310.5	313.1	2.6
Bare Wo - CL2	311.1	314.7	3.6
Bare Wo - CL3	311.4	316.2	4.8
GB Wo - Clean	315.5	320.4	4.9
GB Wo - CL2	316.3	322.4	6.1
GB Wo - CL3	316.2	322.1	5.9
UFB Wo - Clean	319.4	323.3	3.9
UFB Wo - CL2	319.8	324.1	4.3
UFB Wo - CL3	319.1	323.8	4.7

show greater dip in the emissivity spectra. Different contamination levels did not significantly change the spectral emissivity in most cases with the exception of bare aluminum and glossy black aluminum.

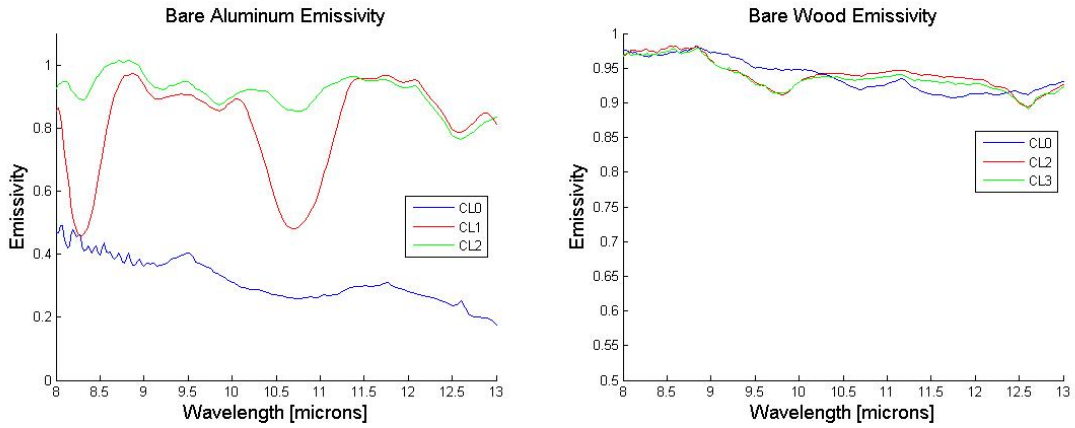

(a) (b)

Figure 4.7: D&P retrieved spectral emissivity of bare aluminum (a) and bare wood (b) samples with SF96 applied.

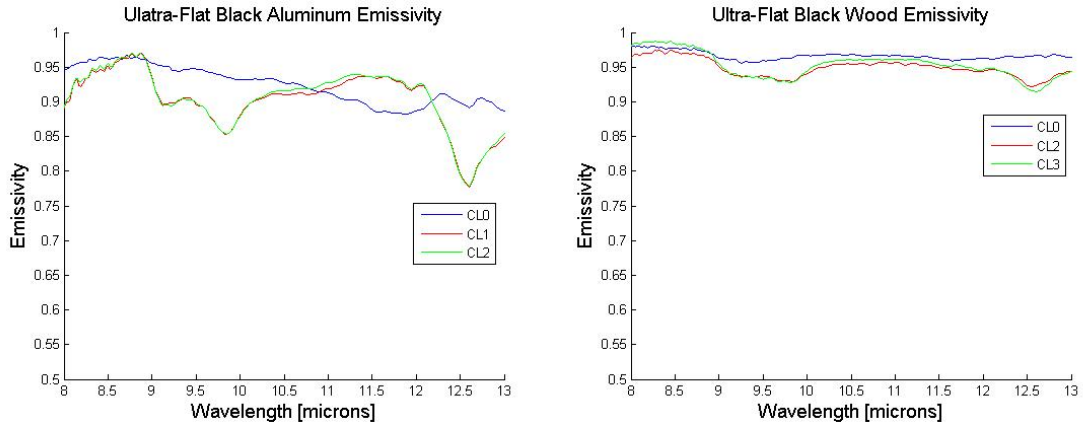

(a) (b)

Figure 4.8: D&P retrieved spectral emissivity of ultra-flat black aluminum (a) and ultra-flat black wood (b) samples with SF96 applied.

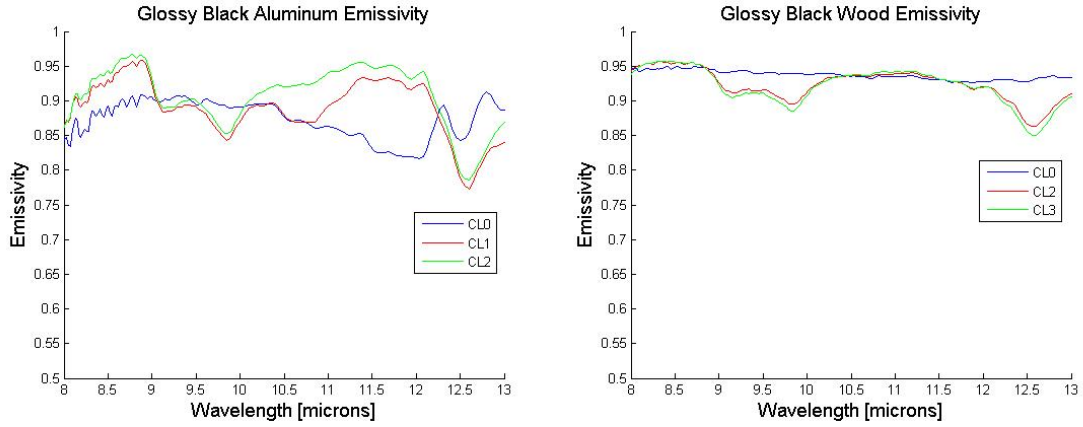

(a) (b)

Figure 4.9: D&P retrieved spectral emissivity of glossy black aluminum (a) and glossy black wood (b) samples with SF96 applied.

The measurement for bare aluminum seemed to show a very inconsistent result. As shown in Table 4.1, the retrieved temperature was computed to 343.4 degrees Kelvin, which was significantly higher than the measured temperature. This inaccuracy was likely

due to the high reflective properties of the sample as shown in Figure 4.10. The calibrated spectral radiance of bare aluminum closely resembled the downwelling radiance as reflected by the infragold plate.

(a)

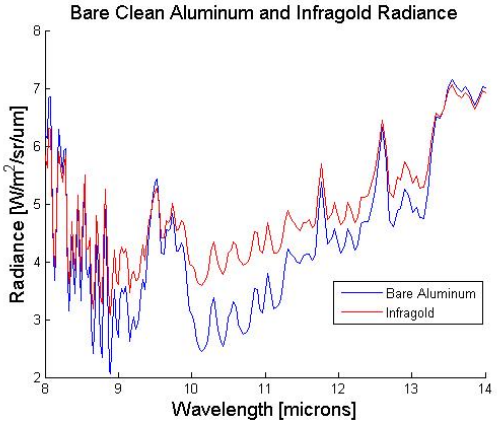

(b)

Figure 4.10: RGB image of bare aluminum sample (a) that appears mirror like and the calibrated measured radiance of the sample compared to the downwelling radiance obtained from the infragold measurement (b).

4.2.4 Error Propagation

An error analysis was also performed on the D&P model 102 measurements to determine the accuracy of the final emissivity curves and to determine the potential contributions of error from each computational step. This was done using the standard method of error propagation by defining a dependent variable (i.e. emissivity) in terms of independent variables that all contribute error due to measurement variability, instrument precision, etc [30]. In a general case, this can be represented by

$$Y = f(X_1, X_2, ..., X_N), \tag{4.7}$$

Table 4.2: Instrument precision parameters

Parameter	Instrument	Value	Units
Wavelength	D&P Model 102	+/- 0.1	microns
BB Temp	D&P Model 102	+/- 0.1	Kelvin
DWR Temp	Exergen Thermometer	+/- 0.1	Kelvin
Sample Temp	Exergen Thermometer	+/- 0.1	Kelvin

with the error (standard deviation) in Y represented as

$$S_Y = \left[\left(\frac{\delta Y}{\delta X_1} S_{X1} \right)^2 + \left(\frac{\delta Y}{\delta X_2} S_{X2} \right)^2 + ... \left(\frac{\delta Y}{\delta X_N} S_{XN} \right)^2 \right]^{1/2}. \tag{4.8}$$

This method was executed on all data processing steps for the D&P measurements (4.1-4.6). A flow chart of these steps is presented in Figure 4.11. The initial inputs were instrument wavelength and blackbody temperature precision values obtained from the D&P model 102 manual [26]. Step 1 applied equation 4.8 to the Planck equation for computing the blackbody spectral radiance at the user set blackbody temperatures with a +/- root-mean-square (RMS) error. The outputs for this step were then inputs within the next processing step, along with any other relevant inputs from the measurements. The +/- RMS error was propagated through every processing step resulting in a final emissivity error.

This analysis revealed that the largest source of error was the accuracy of the temperature measurement/estimation within the TES algorithm. Figure 4.12 provides an example of the error analysis output (a) and the spectral emissivity computed at the measured, retrieved, and a third arbitrary temperature about 2 degrees Kelvin higher than the retrieved temperature (b) for the ultra-flat black aluminum sample at contamination level 1. The

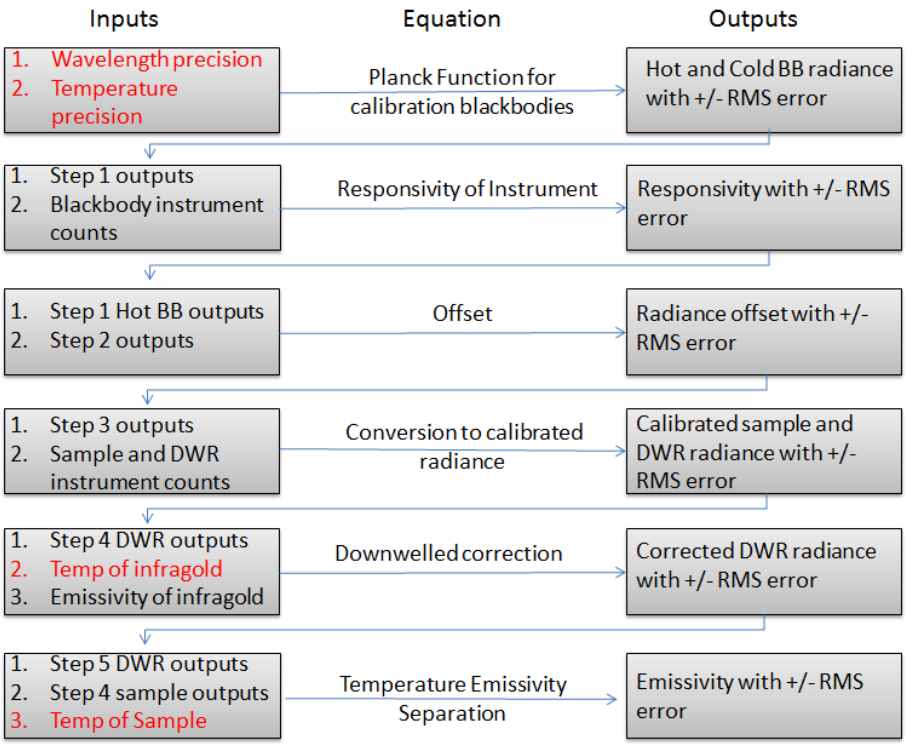

Figure 4.11: Flow chart of error propagation calculation for D&P measurements. Inputs labeled in red are sensor precision values obtained from [26] and [27]. The values of these parameters are listed in Table 4.2

figure shows that the fluctuation in the temperature within the TES algorithm significantly affected the magnitude of the derived spectral emissivity and led to a majority of the error.

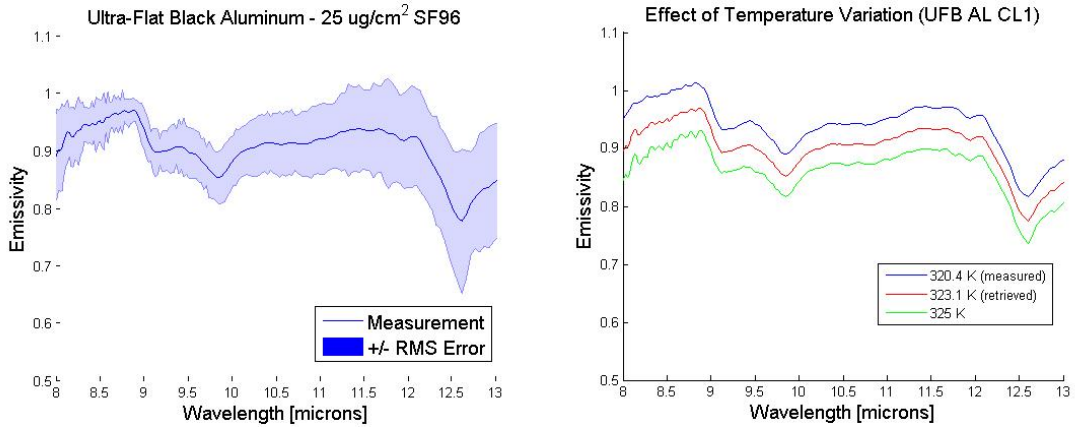

(a) (b)

Figure 4.12: Error analysis output for the ultra-flat black aluminum sample with 25 $\frac{\mu g}{cm^2}$ SF96 applied (a) and emissivity variation when computed at the retrieved temperature, measured temperature, and a 2 degree Kelvin overestimated temperature (b).

Another potential source of error was the fluctuation in the downwelling measurement. Downwelling radiance varied significantly throughout the day. Each emissivity spectra was computed using the closest time matched downwelling measurement; however downwelling radiance was not measured for every sample. Figure 4.13 shows the fluctuation in the downwelling measurement and how the downwelling radiance may affect a measurement. The emissivity spectra are very similar in overall magnitude but differ with respect to the depth of the SF96 features.

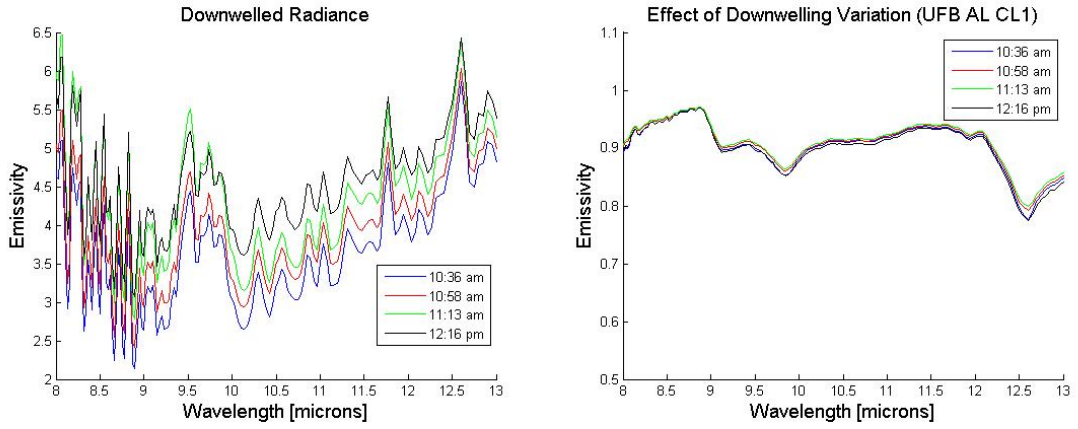

(a) (b)

Figure 4.13: Fluctuation in downwelling radiance measurement with respect to time (a) and the effect on the derived spectral emissivity (b).

4.2.5 Model 102 FTIR Spatial Response Functions

The D&P model 102 produces a single pixel output spectra over the instrument field of view. Therefore, an important consideration when measuring contaminants on surfaces is the spatial response functions of the instrument. Given a 4.8 degree field of view, the D&P model 102 produces a spot size of approximately 3.5 inches in diameter at a height of 42 inches from a nadir viewing angle. Since the output is an averaged spectra over that spot size, this brings up an interesting question of whether the spectra would differ significantly depending on the exact location of the contaminant within the field of view.

The spatial response functions were measured by creating a split sample with thermal contrast, and scanning this sample across the stationary field of view of the instrument [34]. This split sample (Figure 4.14) was created by attaching a bare sheet of aluminum to an ultra-flat black painted aluminum sheet. The different paint finishes created a significant thermal contrast of around 16-19 degrees Celsius (Table 4.3). This contrast lead to a significantly higher measured radiance for the ultra-flat black region as shown in Figure 4.15. The sample was slid across horizontally and vertically in half inch intervals through

the D&P model 102 field of view and the radiance was measured at 9 different positions for each set of measurements. A ruler was used to measure the position of the sample edge and the fraction of each sample within the spot size was computed for each position.

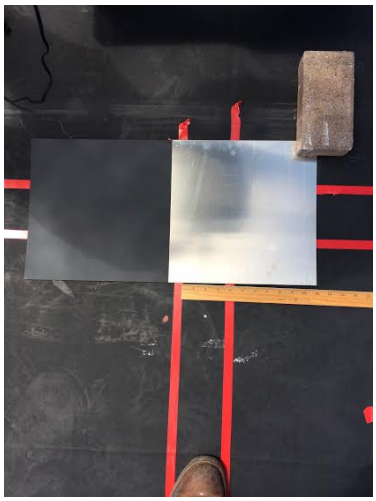

Figure 4.14: Split sample created for measuring the edge response function. The left sample is aluminum with Krylon ultra-flat black paint and the right sample is bare aluminum

Table 4.3: Measured sample temperatures for Edge response function

Sample Fraction (Bare%/UFB%)	Bare Aluminum Temp	UFB Aluminum Temp
100/0	21.1	N/A
100/0	21.4	N/A
100/0	22.1	N/A
91/9	20.8	40.9
77/23	21.0	37.2
41/59	21.1	38.2
59/41	20.7	37.7
23/77	20.5	39.3
9/91	20.2	39.6
0/100	N/A	39.3
0/100	N/A	39.4
0/100	N/A	39.0

The measured radiance was plotted as a function of edge location at each individual wavelength. Figure 4.16 represents the measured data points for the average measured radiance over the LWIR region with a trend line fit. The trend line is an approximated Gauss error function that was fit by a nonlinear least squares regression. The point spread function of the D&P FTIR can then be approximated by differentiating this edge spread function [34]. Figure 4.17 displays the measured PSF cross sections for the D&P FTIR. The measured and fitted PSFs offer insight on how the spectra is averaged within the field of view of the instrument.

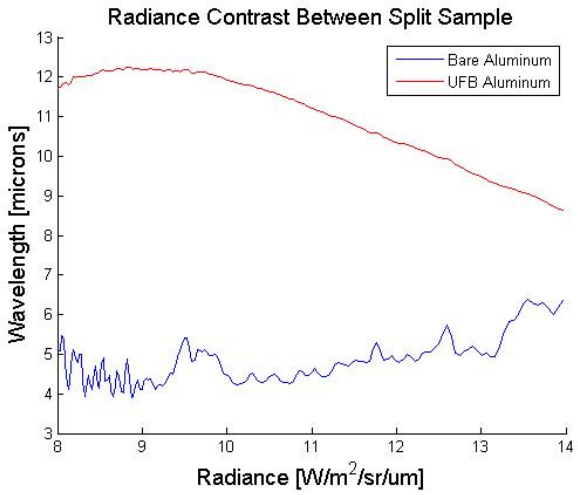

Figure 4.15: Radiance contrast between of samples used to create split sample

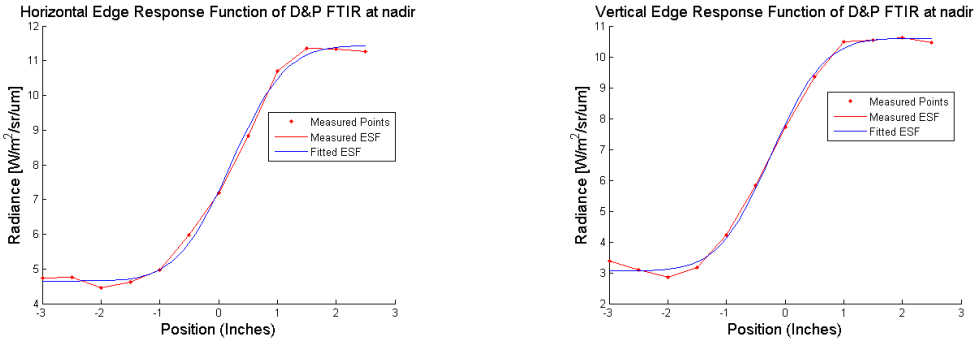

(a) (b)

Figure 4.16: Horizontal (a) and vertical (b) cross section of measured (red) and fitted (blue) edge response functions for the D&P FTIR

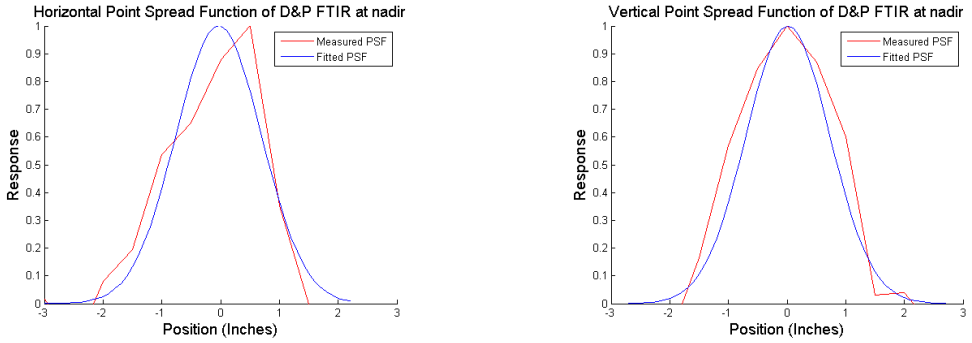

(a) (b)

Figure 4.17: Horizontal (a) and vertical (b) cross section of measured (red) and fitted (blue) point spread functions for the D&P FTIR

4.3 Adaptive Infrared Imaging Spectroradiometer

The AIRIS sensor is an imaging multispectral sensor that has been successfully tested for the detection of chemical and biological agent simulants. This sensor contains a 256x256 pixel wide area detector and provides a 32x32 degree field of view with 10 km spatial resolution at a range of 5 km. The optical configuration is a tunable Fabry Perot interferometer that affords high optical throughput and high spectral resolution along 8-11 μm region [31].

The instrument is equipped with a sensor unit, and operator display unit, a remote data computer, a power unit, and a portable wireless data telemetry and control assembly as shown in Figure 4.18. The instrument utilizes a real-time integrated processor that can perform automated target recognition algorithms on scenes that do not require a priori knowledge. The AIRIS instrument was set up on a tripod that rested in a box truck at a height of about 8 feet. The viewing angle of the instrument was approximately 75 degree off-nadir for all sample measurements.

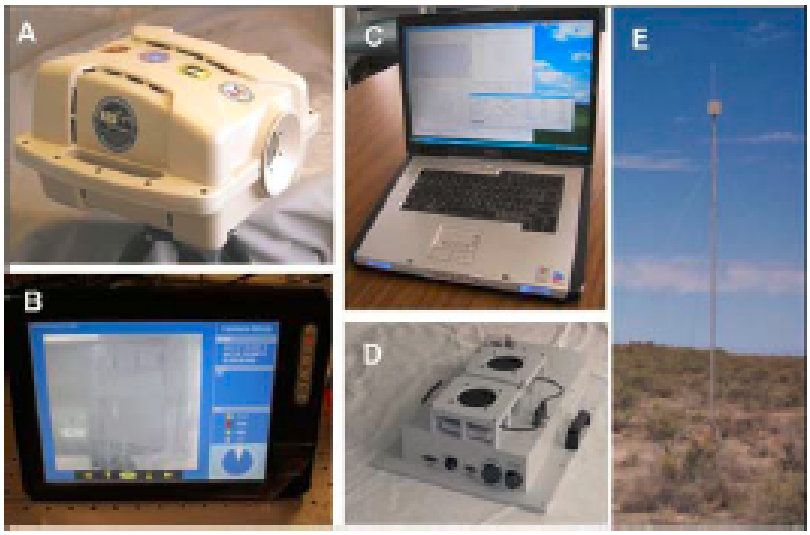

Figure 4.18: AIRIS components: (A) sensor unit, (B) operator display unit, (C) remote data computer, (D) power unit, (E) portable wireless data telemetry and control assembly. [31]

4.3.1 Downwelled Radiance

Downwelled radiance was not measured with the AIRIS sensor during the Andover data collect, however it remains a crucial piece of information when performing the temperature emissivity separation. The infragold measurements from the D&P model 102 were resampled to correspond to the AIRIS band centers by a convolution with an approximation of the AIRIS spectral response function. The AIRIS instrument contained 32 spectral bands ranging from approximately 8-11 μm with varying full width half max ($FWHM$) parameters which are provided in Figure 4.19 in wavenumbers (ν).

The first step was converting the $FWHM$ from wave numbers to wavelength in units

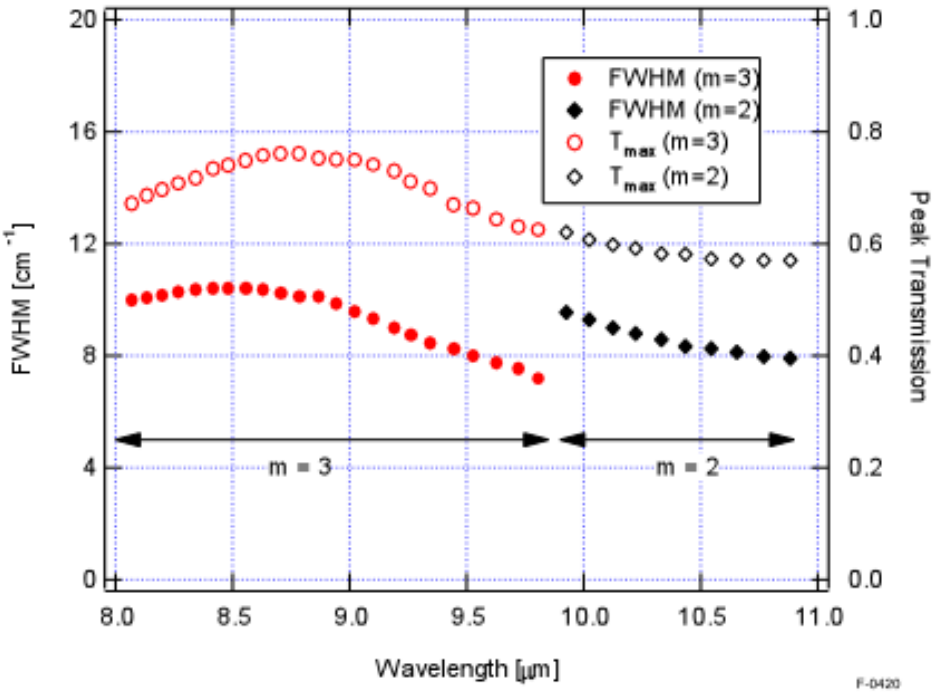

Figure 4.19: FWHM and peak transmission of AIRIS. [31]

of microns by the following relationship

$$FWHM_{\mu m} = \frac{10000 * FWHM_{\nu}}{\nu^2_{AIRIS}}, \tag{4.9}$$

where the denominator denotes the AIRIS band centers in wavenumbers. The AIRIS spectral response function was approximated by assuming a Gaussian shape at each band center which was characterized by its standard deviation. Standard deviation varies depending on the $FWHM_{\mu m}$ and can be computed by the following

$$\sigma = \frac{FWHM_{\mu m}}{2\sqrt{2\ln 2}}. \tag{4.10}$$

The measured downwelled radiance from the D&P model 102 was not sampled at equal

intervals with respect to wavelength. Therefore, the average $\Delta\lambda$ was computed over the spectral range of 8-11 μm and the measured downwelled radiance was interpolated to evenly sampled wavelength, λ_{DOWN}.

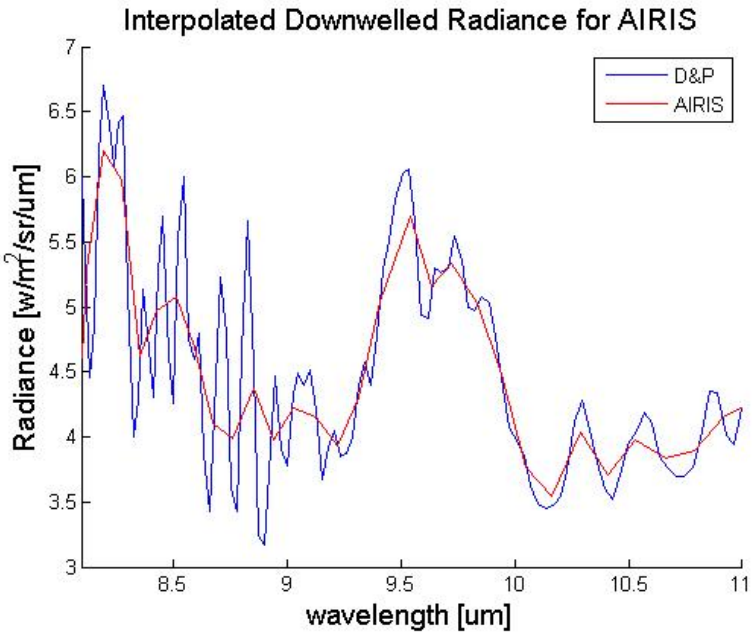

Figure 4.20: Interpolated Downwelled Radiance for AIRIS

4.3.2 TES

The interpolated downwelling radiance allowed us to derive the spectral emissivity of the samples from the AIRIS radiance data. Emissivity spectra derived from the TES algorithm did not show consistent results for the AIRIS data. The emissivity spectra in relation to the D&P spectra seemed to show similar features for the aluminum cases, however these features were less prominent. The wood samples did not seem to show a noticeable difference between the clean and contaminated samples. Figures 4.21-4.23 show each AIRIS contaminant and paint sample measurement combination.

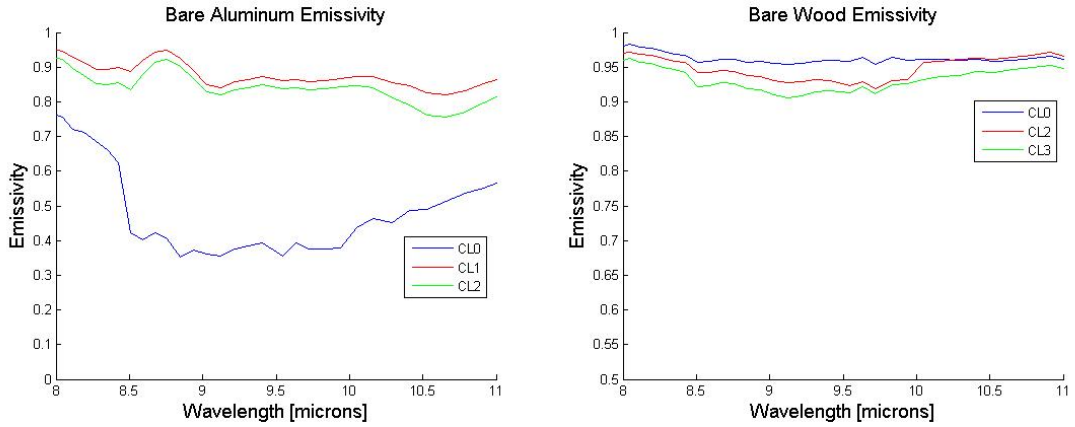

(a) (b)

Figure 4.21: AIRIS retrieved spectral emissivity of bare aluminum (a) and bare wood (b) samples with SF96 applied.

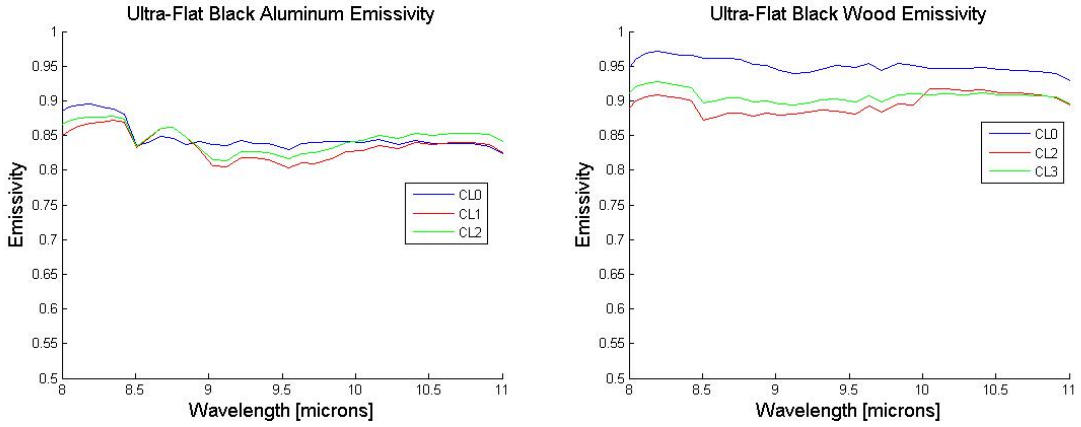

(a) (b)

Figure 4.22: AIRIS retrieved spectral emissivity of ultra-flat black aluminum (a) and ultra-flat black wood (b) samples with SF96 applied.

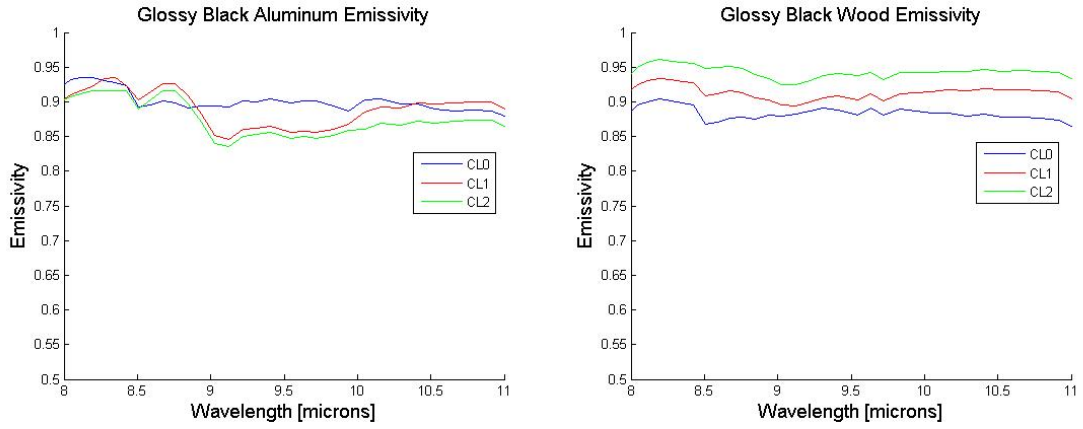

(a) (b)

Figure 4.23: AIRIS retrieved spectral emissivity of glossy black aluminum (a) and glossy black wood (b) samples with SF96 applied.

The painted aluminum plots did faintly show the SF96 spectral feature between the 9 and 10 micron range; however they were much less defined then the model predictions. Wood samples were consistently flat and all measurements were spectrally similar with and without the contaminant. Inaccuracies may have been caused due to the fundamental assumptions within the TES algorithm. The TES algorithm assumed a spatially and spectrally uniform transmission of 1 and a negligible path radiance, which most likely was not the case with the target to sensor path length for the AIRIS measurement. The path length for AIRIS was approximately fifteen meters at the location of the samples. A MODTRAN run was executed to verify if the transmission and path radiance met the TES assumption criterion. The path transmission and path radiance are plotted in Figures 4.25 and 4.24. These plots reveal that although the transmission was very close to 1, the path radiance was not negligible and therefore violated the TES assumption.

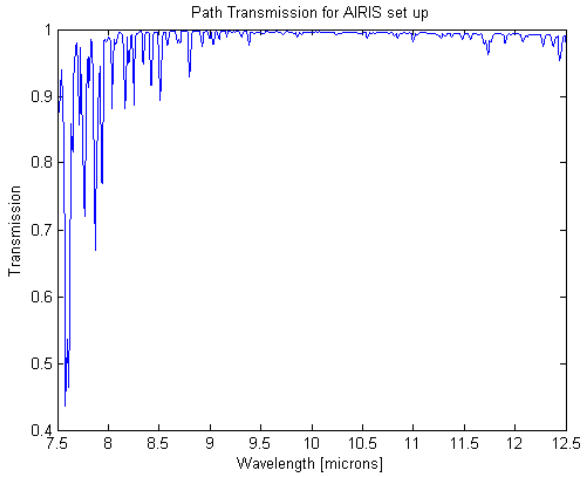

Figure 4.24: MODTRAN computed transmission for the AIRIS measurements scene geometry

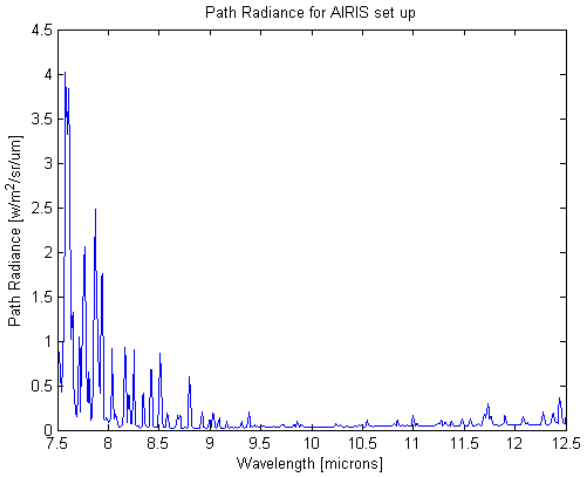

Figure 4.25: MODTRAN computed path radiance for the AIRIS measurements scene geometry

Figure 4.26: Ultra-flat black sample with SF96 applied for angular measurements.

4.4 Additional Measurements

The Andover data collect provided spectra for a variety of surface combinations but did not provide measurements at different viewing angles. Often, the spectra of materials changes drastically at lower viewing angles. Therefore, to provide further measurements for model validation, another ultra-flat black aluminum sample was prepared with SF96 contamination. A weighted amount of the contaminant (0.49 g) was applied to the center of the aluminum plate with a spoon and allowed to naturally disperse over a period of time 4.26. Since the dimensions of the aluminum plate were known (12 by 12 inches) the ground sampled distance could be computed by dividing the number of pixels in the aluminum plate edge by the length of the plate. The contaminant dispersed in an ellipse-like shape and therefore an approximation of the area of the layer was computed by creating a mask in ENVI and determining the amount of pixels within the region. The density of SF96 is a known value (0.79 g/cm^3) and therefore the thickness of the SF96 film was computed to approximately 5.49 microns.

Measurements were taken using the D&P FTIR at a range of viewing angles. The D&P instrument is conventionally mounted on a tripod which limits the height at which measurements may taken above the sample. For the angular measurements, a new mount

was constructed that allowed for vertical adjustment. This setup allowed for consistency in the relative spot size diameter on the sample as the viewing angle was changed. Each measurement was aligned so that the instrument field of view was over only the contaminant region. Measurements were taken from nadir to 75° off nadir at 15° increments. Blackbody radiance and downwelled radiance curves were measured for every sample measurement as an attempt to eliminate any error obtained from thermal drift or changes in sky conditions. Figure 4.27 displays the measured radiance and extracted emissivity for the sample (4.26) at different viewing angles. An immediate visual observation is the change in the spectral features from 9 to 10 microns as the viewing angle becomes more oblique. Both plots show a decreasing overall trend and a distinct increase in the depth of the absorption feature around 9 microns.

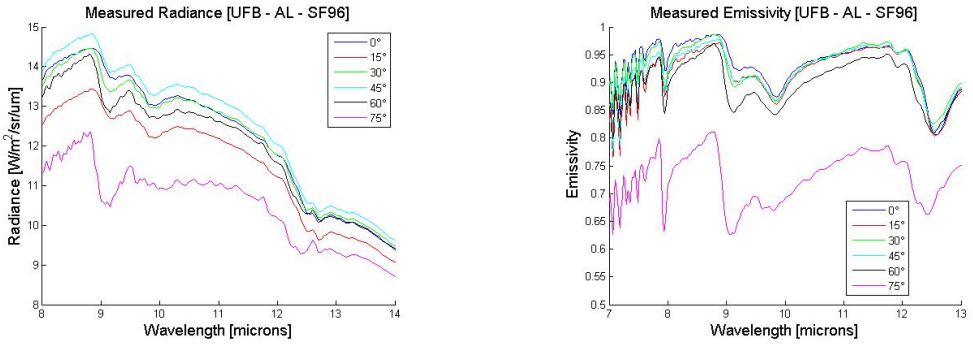

(a) (b)

Figure 4.27: Measured radiance (a) and derived emissivity (b) of ultra-flat black aluminum sample with 5 micron thick layer of SF96 applied

4.5 Chapter Summary

This chapter provided context on an experiment designed to obtain reliable measurements of liquid-contaminated surfaces. Well characterized samples were prepared and radiance in the LWIR was measured with two different instruments. These measurements were

taken in order to validate a radiative transfer BRDF model. The radiance spectra from both instruments was processed to extract the surface parameter emissivity for model comparisons in both the radiance and emissivity domains.

Chapter 5

Model Validation

The chapter provides initial results of comparisons between the empirical measurements and microDIRSIG model predicted spectra. Emissivity and radiance were the fundamental parameters used in comparison. Radiance was empirically measured by the D&P model 102 and AIRIS instruments and also generated synthetically by DIRSIG. Emissivity was retrieved from the measured radiance by use of a TES algorithm as well as generated numerically from the microDIRSIG model. Other other important parameters included the sample temperature and the downwelling radiance which were also measured. The utilization of well characterized surfaces also allowed for measurement validation with The Nonconventional Exploitation Factors Data System (NEFDS) [23]. This database contains measured and computed surface reflection parameters for a variety of different materials. Section 5.1 provides comparison in the emissivity domain and section 5.2 provides comparisons of spectral radiance in an effort to validate the microDIRSIG model.

5.1 Emissivity Comparisons

A majority of the measured and model predicted spectral comparisons were done in the emissivity domain. This section provides the results for three sets of emissivity spectra

comparisons. Not considered specifically for model validation, the first comparison was made between the D&P emissivity and the Nonconventional Exploitation Factors Data System (NEF)database for the clean samples. The next two sets of comparisons are between the different instruments measurements and the microDIRSIG model predicted outputs.

5.1.1 NEFDS vs D&P Emissivity

The samples that were chosen had a mature characterization history within the NEF without the presence of a contaminant and therefore the bare material measurements were first compared against the database. This comparison was meant to verify the accuracy of the measurements. The five samples presented in Figures 5.1 and 5.2 did show a reasonable agreement with the expectations of the NEF database. The bare aluminum sample was ignored due the inability to accurately extract emissivity and sample temperature. Due to the highly reflective nature of the sample, the measured radiance was very similar to the sky emitted radiance, thus violating the fundamental constraint on the TES algorithm. The TES algorithm requires an accurate retrieval of a surface temperature and a noticeable separation between the magnitude of the sample and background (downwelled) radiance to accurately compute emissivity [28] [29]. The measured emissivity spectra (blue) are plotted with a +/- root-mean-square uncertainty region to convey a sense of confidence bounds associated with the measured values at each wavelength. This was computed by using the standard method of error propagation through all data processing steps as described in 4.2.4. The measured and retrieved temperature variation was the largest source of error. The D&P measurements were generally very similar to the NEFDS curves and are shown in figures 5.1 and 5.2.

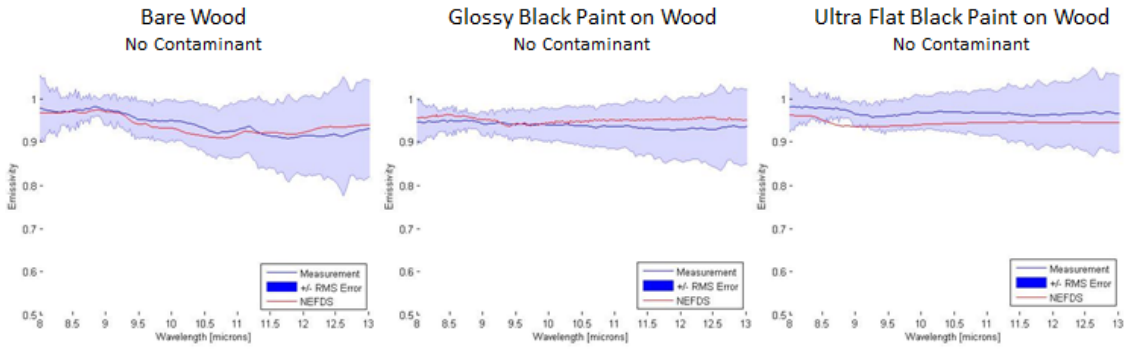

Figure 5.1: NEF database (red curves) and measurement derived emissivity spectra (blue curves) for all three uncontaminated wood surface types.

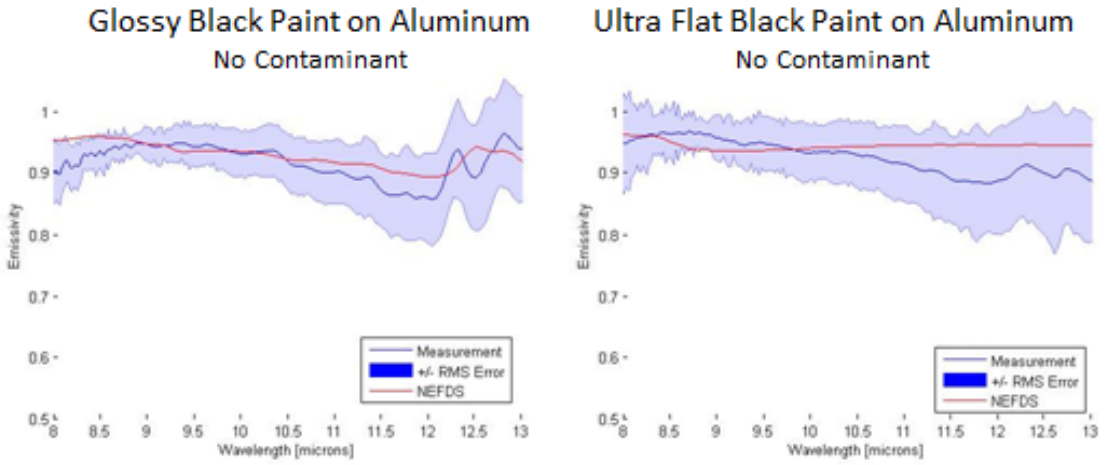

Figure 5.2: NEF database (red curves) and measurement derived emissivity spectra (blue curves) for both painted aluminum surface types. The unpainted aluminum measurements are not presented, in that the emissivity is very low and does not conform well to the assumptions of the TES algorithm used.

5.1.2 D&P vs microDIRSIG Emissivity

A majority of the model validation was done with comparisons in the emissivity domain and are shown in Figures 5.3 - 5.5. The measured emissivity spectra (blue) are plotted with a +/- root-mean-square and the model predicted emissivity (red) is plotted with a region of polarization variation that may have arisen due to uncertainty with sensor polarization sensitivity. Specifically, the solid red line represents the in-sensitive incident radiance polarization state. The shaded region represents a range of which the spectrometer is sensitive to only horizontally or only vertically polarized incident radiance.

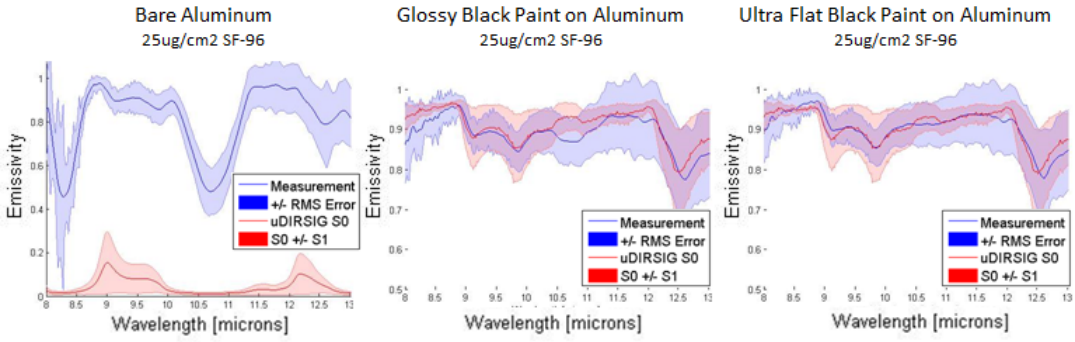

Figure 5.3: microDIRSIG modeled (red) and field measured emissivity spectra (blue) for 25 ug/cm2 of SF96 deposited on three different aluminum plate surface coatings.

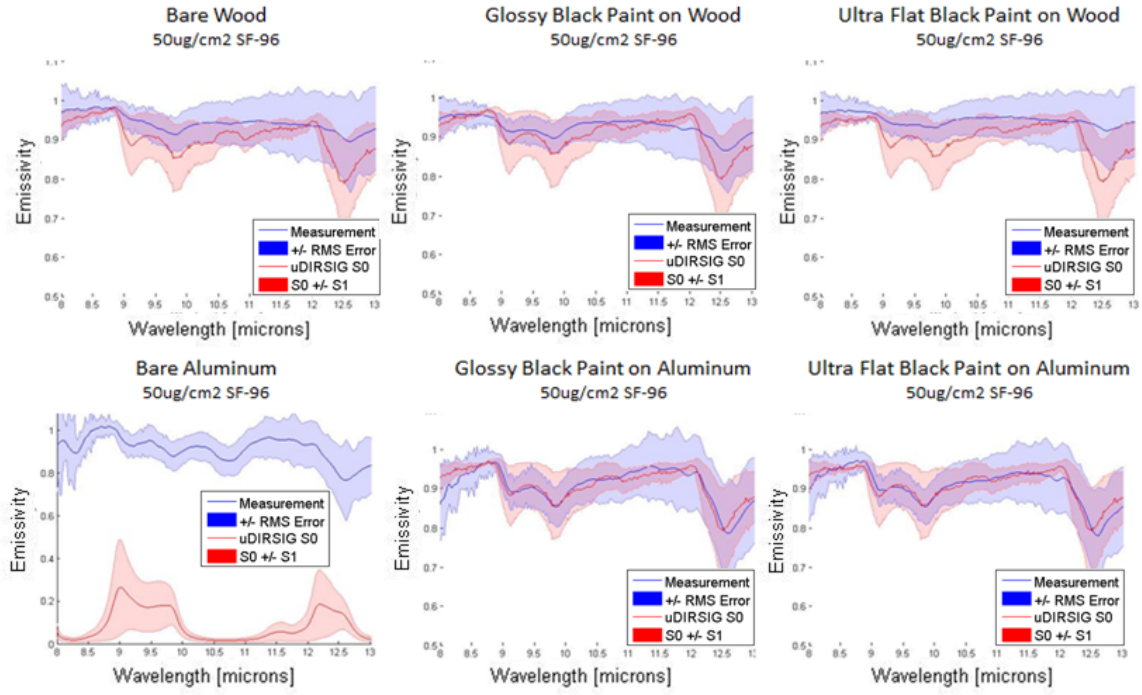

Figure 5.4: microDIRSIG modeled (red) and field measured emissivity spectra (blue) for 50 ug/cm2 of SF96 deposited on three different aluminum plate surface coatings and three different wood surface coatings.

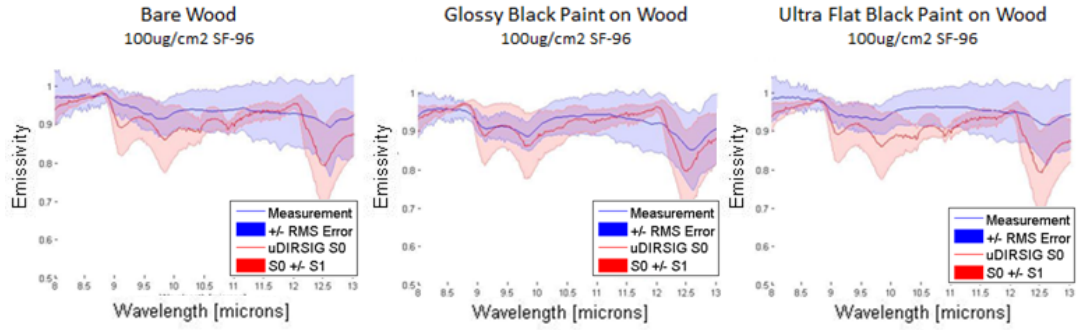

Figure 5.5: microDIRSIG modeled (red) and field measured emissivity spectra (blue) for 100 ug/cm2 of SF96 deposited on three different wood surface coatings.

Visually, the best agreement between the microDIRSIG predicted emissivity and the field measured emissivity were for the ultra-flat black and glossy black aluminum samples with 25 and 50 ug/cm^2 of SF96 applied. The microDIRSIG output was almost exclusively located within the D&P error bounds for the painted aluminum cases. Measured emissivity spectra of the contaminated wood samples seemed to show the SF96 features and were spectrally similar in shape, however the features were less defined when compared to the model and the aluminum samples. The microscopic images did show that many cracks or gaps were present in the paint coating on the wood surfaces. This was likely due to the grain structure of the wood and the porous nature of the wood as a substrate. The wood was modeled as a homogeneous surface which may have attributed to the slight mismatch of the measured and predicted curves.

The bare aluminum samples resulted in a poor agreement with the model and had no overlap between the measured and predicted confidence bounds. This is likely due to the inaccuracies in the TES that may have arisen because of the highly specular properties of the bare aluminum samples, which violates the diffuse downwelled assumption. Model performance was quantitatively analyzed by utilizing the Spectral Angle Mapper (SAM) algorithm. The magnitude of the spectral angle for all samples is displayed in Figure 5.6 and results confirm the visual comparison.

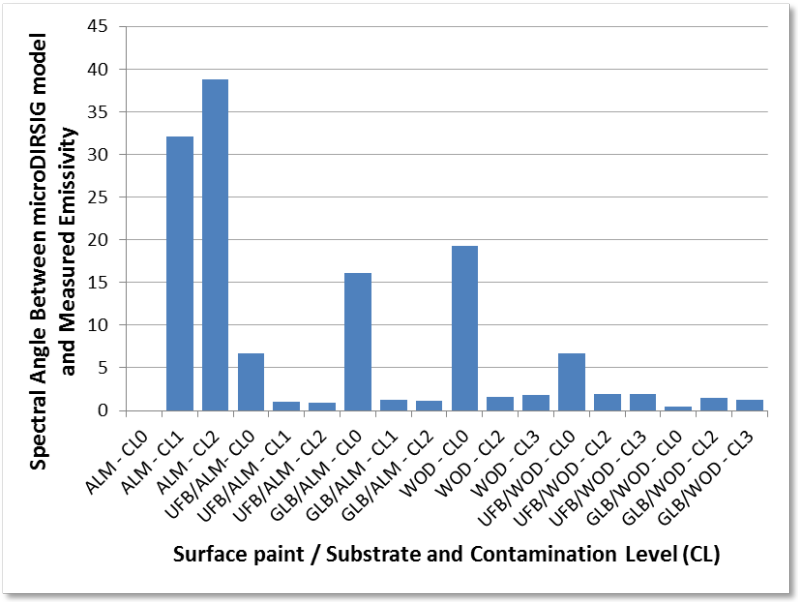

Figure 5.6: Summary of the spectral angle between modeled and measured emissivity spectra for the surface substrates, paint coatings, and contamination levels considered (CL0: no SF96, CL1: 25 ug/cm2 SF96, CL2: 50 ug/cm2 SF96, CL3: 100ug/cm2 SF96).

The additional angular measurements of the ultra-flat black aluminum sample with SF96 also showed a good agreement with the modeled spectra. Both the model predicted and measured emissivity spectra displayed an overall decrease in the magnitude of the spectra and an increase in the spectral absorption feature at 9 microns (Figure 4.26). The quantitative comparison showed spectral angles that ranged from around 0.7° to 3° and RMS error that ranged from 0.02 to 0.03 (Table 5.1). As the zenith angle increased, the spectral angle and the RMS error both increased. The RMS error between the sample measurement and the model outputs were within computed error bounds of the measurements and therefore the model was validated for the ultra-flat black aluminum sample with SF96.

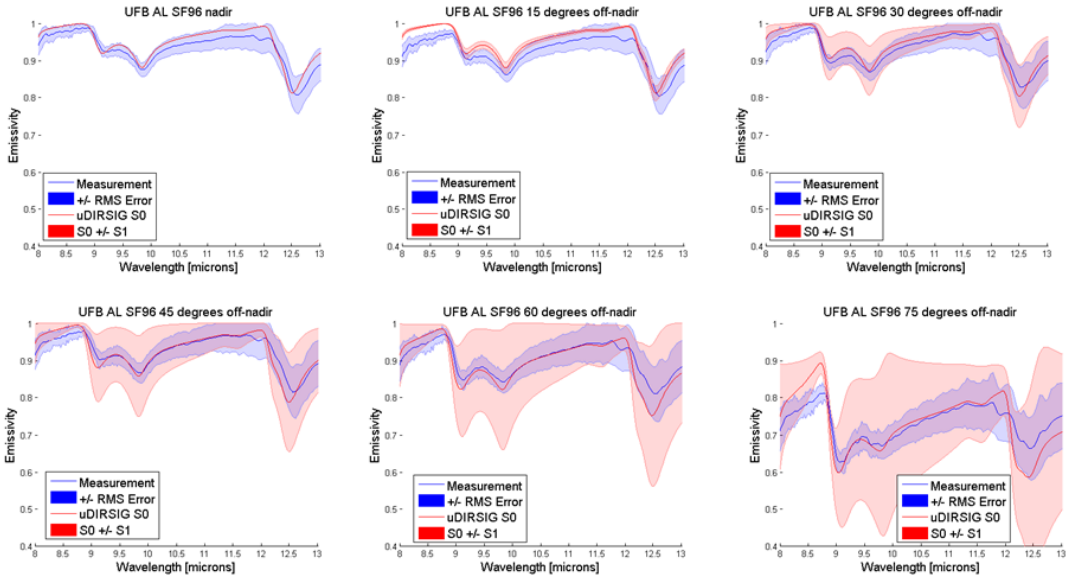

Figure 5.7: Comparison of microDIRSIG modeled emissivity and D&P FTIR measured emissivity at different zenith viewing angles for an ultra-flat black aluminum sample with a 5 micron thick layer of SF96

Table 5.1: Spectral angle and RMS error between microDIRSIG modeled emissivity and measured emissivity and the propagated measurement error at different viewing angles for ultra-flat black aluminum with a 5 micron thick layer of SF96

Viewing Angle	SAM (deg)	RMS (emissivity)	Measurement Error (emissivity)
nadir	0.6996	0.0172	0.0274
15°	0.7165	0.0262	0.0293
30°	0.7045	0.0168	0.0328
45°	1.1240	0.0184	0.0383
60°	1.4366	0.0231	0.0438
75°	2.9923	0.0396	0.0547

5.1.3 AIRIS vs microDIRSIG Emissivity

The AIRIS data did not show promising agreement between the microDIRSIG outputs in either the emissivity or the radiance domain. Calibrated AIRIS data were provided directly from PSI, which brings up question as to how the data was initially processed. The measured spectra seemed to show similar features to the model predicted outputs for the aluminum, however much less defined (Figures 5.8-5.10). There are several potential sources of error within the AIRIS processing. First, the TES algorithm makes an assumption that the path radiance is negligible and the transmission is one. This assumption applies to the D&P path length which is approximately 1 meter. With the AIRIS sensor being located about 15 meters from the sample, this assumption may not be valid and the TES algorithm did not seem to retrieve accurate emissivity spectra. Also, we were unable to measure the sample temperatures at the exact time of the measurements because the D&P was operated in sync with AIRIS. Because the TES algorithm failed in some cases, the temperature was manually input into the algorithm along with the down sampled downwelled radiance term. Therefore, the retrieved emissivity may not be valid for model validation and further measurements may be required.

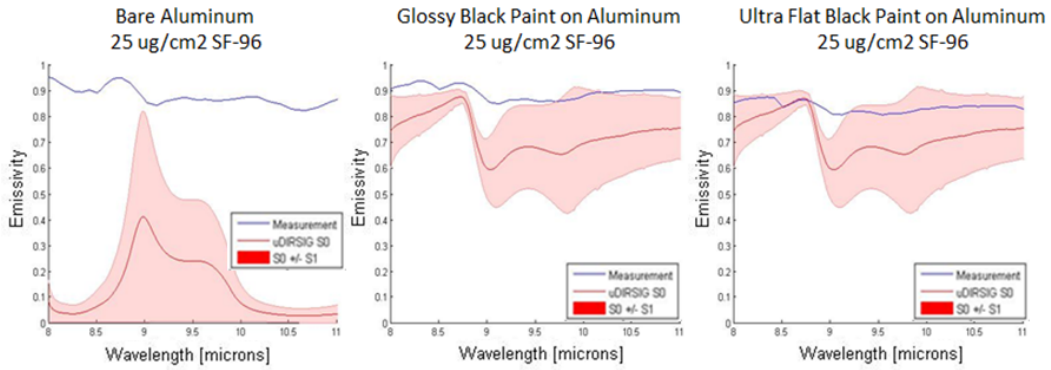

Figure 5.8: microDIRSIG modeled (red) and field measured AIRIS emissivity spectra (blue) for 25 ug/cm2 of SF96 deposited on three different aluminum plate surface coatings.

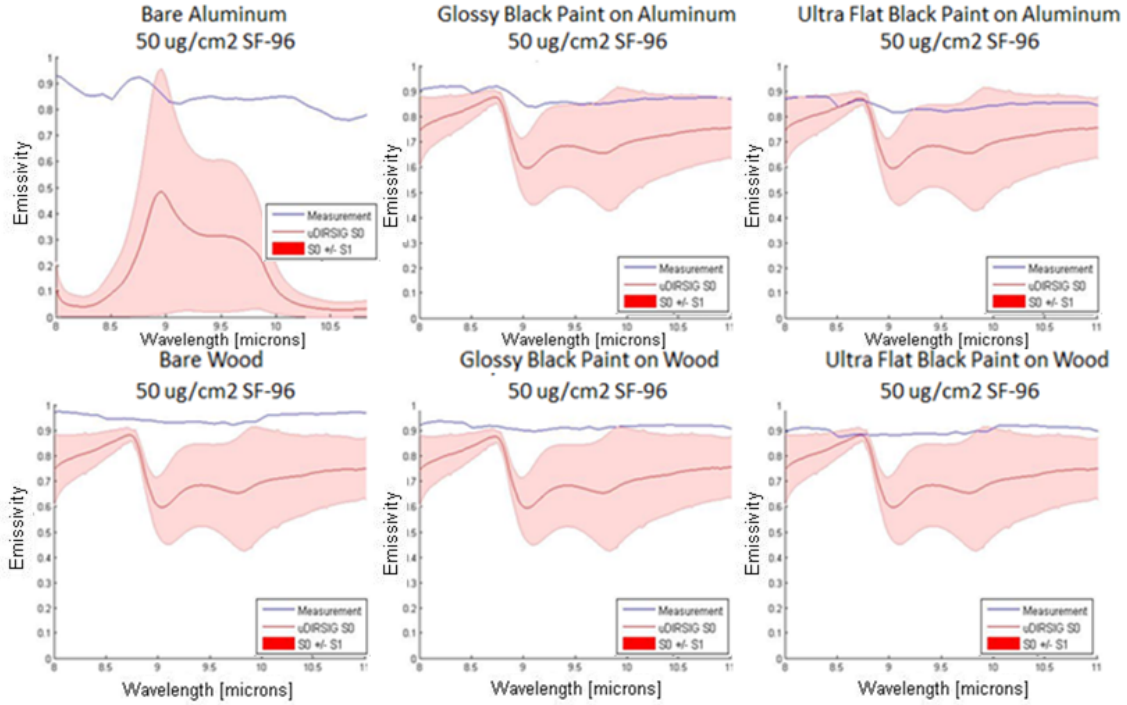

Figure 5.9: microDIRSIG modeled (red) and field measured AIRIS emissivity spectra (blue) for 50 ug/cm2 of SF96 deposited on three different aluminum plate surface coatings and three different wood surface coatings.

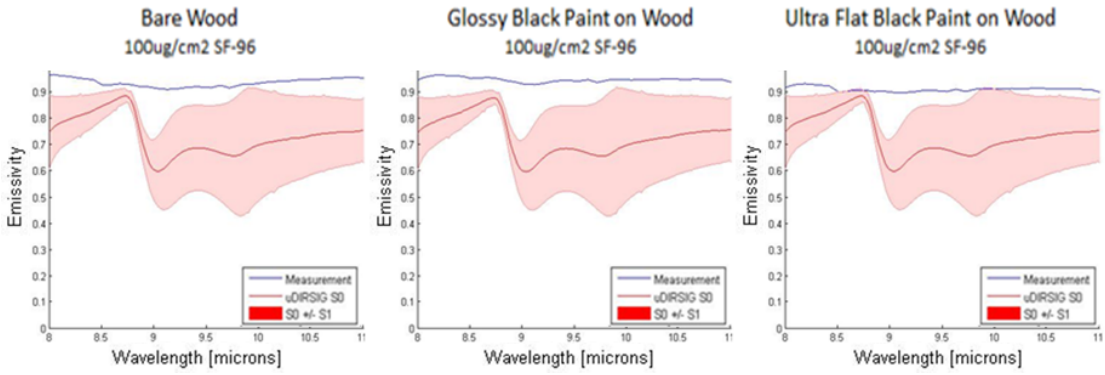

Figure 5.10: microDIRSIG modeled (red) and field measured AIRIS emissivity spectra (blue) for 100 ug/cm2 of SF96 deposited on three different aluminum plate surface coatings.

5.2 Radiance Comparisons

The Digital Imaging and Remote Sensing Image Generation (DIRSIG) model is a first-principles based radiation propagation model used to generate synthetic imagery datasets for a variety of different modalities. All modalities are simulated from imported 3-D geometric scenes constructed in computer aided design programs. Materials within the scene may be attributed with thermodynamic and optical properties to drive radiometric prediction. The atmosphere is characterized by a computer program, MODerate resolution atmospheric TRANsmission (MODTRAN), which is executed directly within DIRSIG. DIRSIG is capable of producing BRDF predictions with several built in BRDF models that have had accurate results when compared to empirical databases [20][23].

A simple three dimensional scene with a similar sample layout as in Figure 4.1 was created in a computer aided design program (Blender) to closely resemble the Andover data collect (Figure 5.11). Retrieved temperatures from the TES algorithm and microDIRSIG emissivity spectra were then input into the material editor within DIRSIG to define the surface properties of each sample. The atmosphere was characterized by executing a

MODTRAN run within DIRSIG and atmospheric conditions such as ambient temperature, humidity, and pressure were specified from weather observations in Andover on the day of the collect. The sensor location and view angle were set within DIRSIG to represent the D&P view angle geometry and an independent DIRSIG run was rendered for each sample.

(a)

Figure 5.11: Top view of blender scene created for DIRSIG simulation (a) and zoomed in view on the aluminum samples (b). The building and trees were placed in the scene to try and create a similar surrounding to the Andover data collect.

5.2.1 D&P FTIR DIRSIG Implementation

The D&P FTIR contains a Michelson interferometer which includes infrared optics, a beam splitter, and a scanning mirror assembly [26]. Light entering the interferometer is directed toward a beam splitter which reflects half the light toward a fixed mirror and transmits half the light toward a moving mirror. This moving mirror is servo driven at a constant speed which is continuously changing the optical path length. The difference in the optical path length of the fixed and moving mirrors represents the retardation. The spectral resolution in wavenumber per cm is equivalent to the reciprocal of the maximum retardation in cm. The instrument often produces multiple interferograms which are then

coadded to bring down system noise. This interferogram is represented in the length domain and can be converted to a spectrum in the wavenumber domain by applying a discrete Fourier transform. Often an apodization step is applied before the fast Fourier transform which is an optical filtering technique that smooths out discontinuities at the beginning and end of the sampled spectrum.

DIRSIG does not currently have an FTIR option built within the graphical user interface. Therefore, replicating the D&P model 102 sensor within DIRSIG required a post interferogram processing technique. The sensor platform was set to a raw spectrometer capture within the platform editor over the LWIR range at 1 wavenumber sampling. The simulation resulted in a radiance output that was much higher sampled (1 cm^{-1}) when compared to the D&P resolution (4 cm^{-1}). The fast Fourier transform of the spectra produced an interferogram containing 4 times as many elements over the LWIR region as the D&P interferogram. The DIRSIG generated interferogram was then truncated to the D&P interferogram width by applying a Hanning window. By taking the fast Fourier transform of the apodized interferogram, a radiance spectrum at the D&P resolution was produced. This spectrum was then converted to per micron for comparison to the measurements. This process is illustrated in Figure 5.12.

The forward modeling results, as expected showed accurate radiance estimations for the aluminum surfaces with a root-mean-square (RMS) error of 0.2086 and 0.2442 $watts/(m^2 - sr - \mu m)$ for the ultra-flat black and glossy black samples respectively with 50 $\mu g/cm^2$ SF96 applied. The wood samples showed reasonable results with RMS differences of 0.5017 and 0.3261 $watts/(m^2 - sr - \mu m)$ for the ultra-flat black and glossy black surfaces at the same contamination level. The RMS error between the modeled and measured radiance fell within the error bounds for the aluminum measurements however did not for the wood measurements. All estimated vs. measured radiance comparisons (Figures 5.13 and 5.14) had spectral angles of about 1 degree as shown in Table 5.2. The measured radiance is also plotted with a +/- RMS radiance error that was computed from

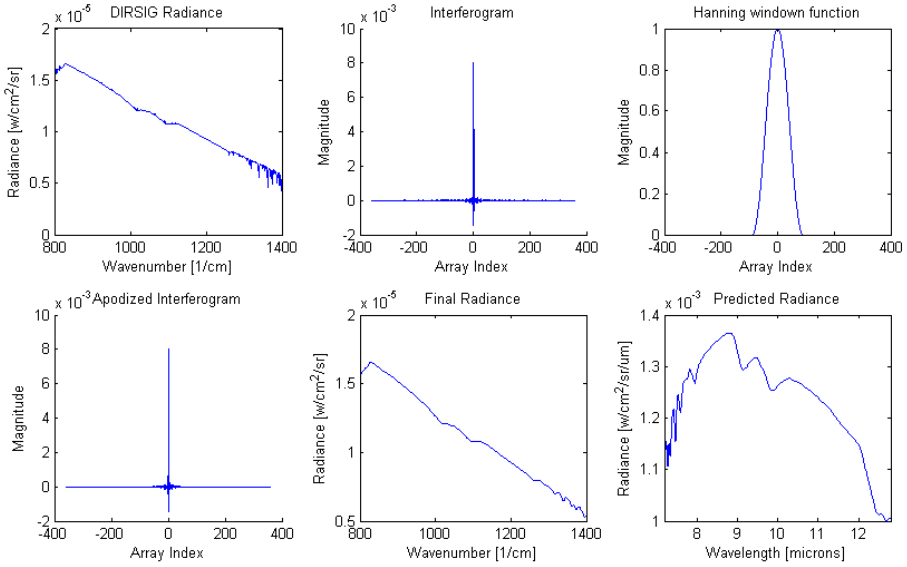

Figure 5.12: From upper left to lower right: 1. DIRSIG generated radiance in wavenumber; 2. Interferogram obtained from taking the FFT of (1); 3. Hanning window function applied to interferogram; 4. Apodized interferogram produced after applying Hanning window; 5. Radiance in wavenumber after interferogram processing; 6. Final predicted radiance converted to per micron.

the process explained in 4.2.4.

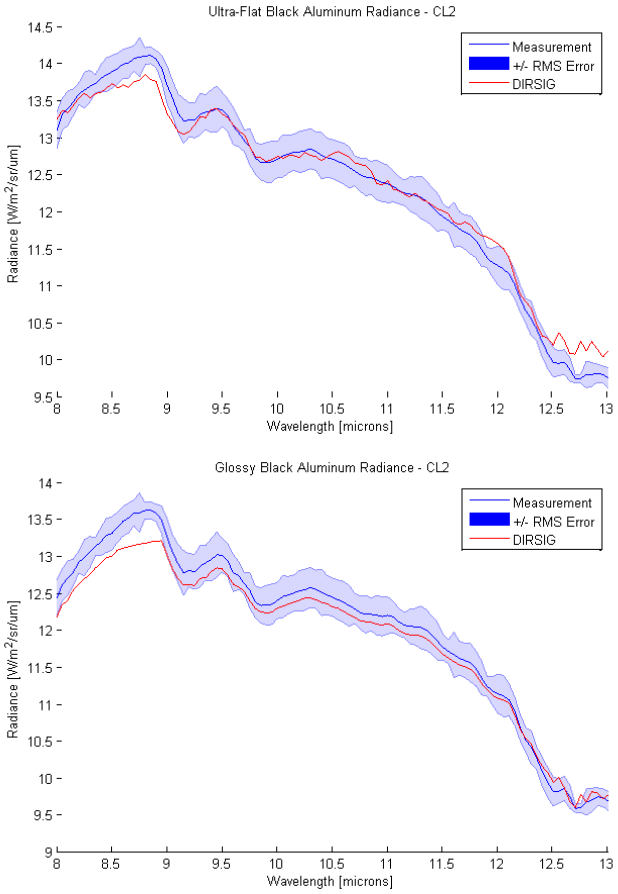

Figure 5.13: Estimated spectral radiance obtained from D&P DIRSIG simulation for ultra-flat black and glossy black aluminum samples with CL2. Sample emissivity was defined using microDIRSIG 45 degree off-nadir model output and temperature of sample was set to retrieved temperature obtained from TES algorithm.

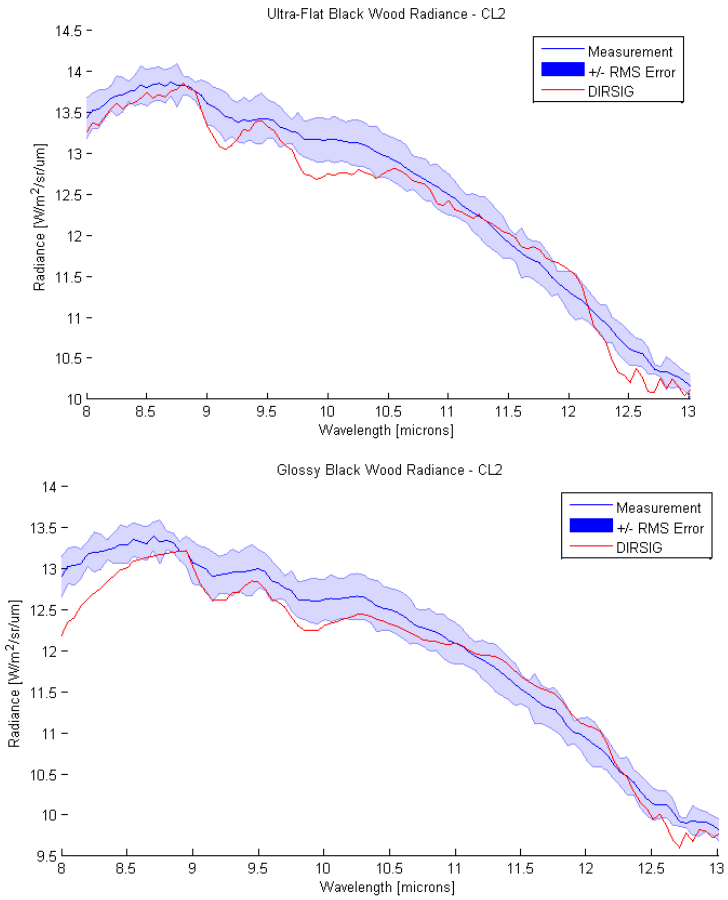

Figure 5.14: Estimated spectral radiance obtained from D&P DIRSIG simulation for ultra-flat black and glossy black wood samples with CL2. Sample emissivity was defined using microDIRSIG 45 degree off-nadir model output and temperature of sample was set to retrieved temperature obtained from TES algorithm.

The angular microDIRSIG spectra outputs were also forward modeled through the DIRSIG simulation for the ultra-flat aluminum with SF96 sample shown in 5.15. Modeled results showed a very promising agreement with the measurements. For all viewing angles, the modeled spectra fell within the error bound computed for the radiance measurements. The RMS error ranged from 0.0774-0.2981 $[W/m^2/sr/\mu m]$ and all spectral angels with

Table 5.2: Spectral angle and RMS error between modeled and measured radiance spectra and computed measurement error $[W/m^2/sr/\mu m]$

Sample	SAM (deg)	RMS Error	Measurement Error
GB WO CL2	1.2671	0.3261	0.2932
UFB WO CL2	1.0620	0.5017	0.3425
GB AL CL2	0.0138	0.2442	0.3093
UFB AL CL2	0.0166	0.2086	0.2912

the exception of the 75° zenith viewing angle fell under 1 degree. As the sensor zenith angle increased, there was a clear trend that was captured in both the modeled and measured results. Similarly to the emissivity comparisons, an absorption feature at 9 microns increased in depth as the angle became more oblique. The magnitude of the radiance also seemed to decrease as the zenith angle increased, which was evident in both sets of radiance spectra.

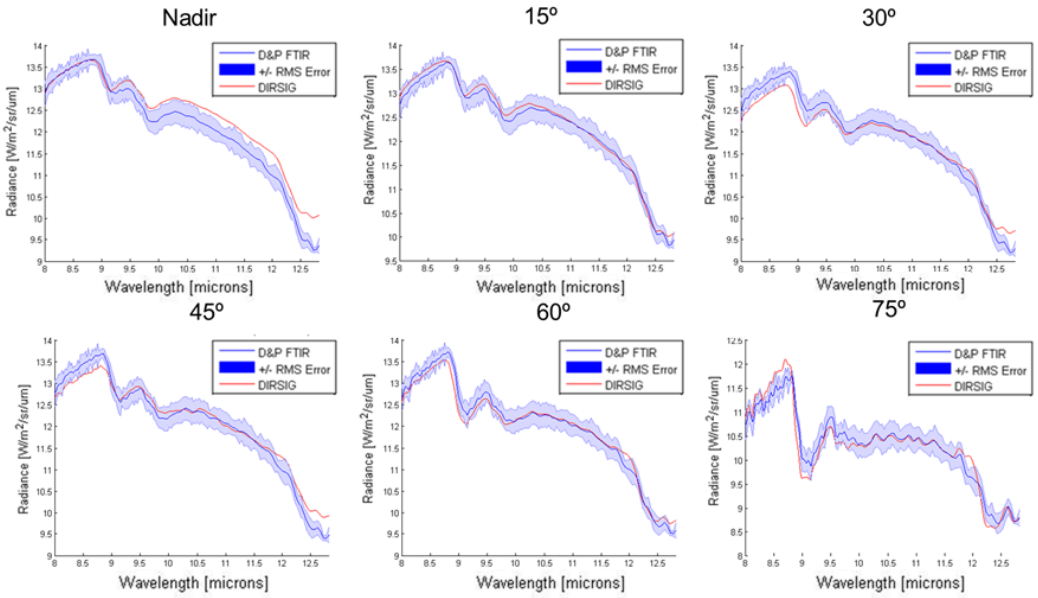

Figure 5.15: Comparison of forward modeled radiance to D&P FTIR measured radiance at different off-nadir sensor viewing angles

Table 5.3: DIRSIG modeled radiance vs measured radiance RMS error in $W/m^2/sr/\mu m$ and spectral angle at different off-nadir sensor viewing angles

Angle	SAM (deg)	RMS Error	Measurement Error (radiance)
nadir	0.8321	0.2981	0.3023
15°	0.3121	0.0774	0.2845
30°	0.9185	0.2320	0.2952
45°	0.6281	0.1463	0.2730
60°	0.6175	0.1509	0.2893
75°	1.2158	0.2233	0.2928

5.2.2 AIRIS Scene Geometry

The forward modeled radiance did not match as well for the AIRIS measured radiance (Figure 5.16) with RMS error of 1.16 $watts/(m^2 - sr - \mu m)$ for the ultra-flat black aluminum and 1.21 $watts/(m^2 - sr - \mu m)$ for the glossy black sample. The radiance spectra seemed to show a similar trend however the magnitude of the radiance curves were significantly off around 9 microns. This brings up question within the model validation. The AIRIS sensor is typically utilized for real-time detection and uses in scene algorithms for separating the background and target radiance [31]. Therefore, the algorithms are applied in the differential radiance domain. The AIRIS sensor has demonstrated success when deployed in the field for chemical detection, however processing uncertainties led to difficulties when trying to correctly model the scene. Further model validation may be required with use of the D&P model 102.

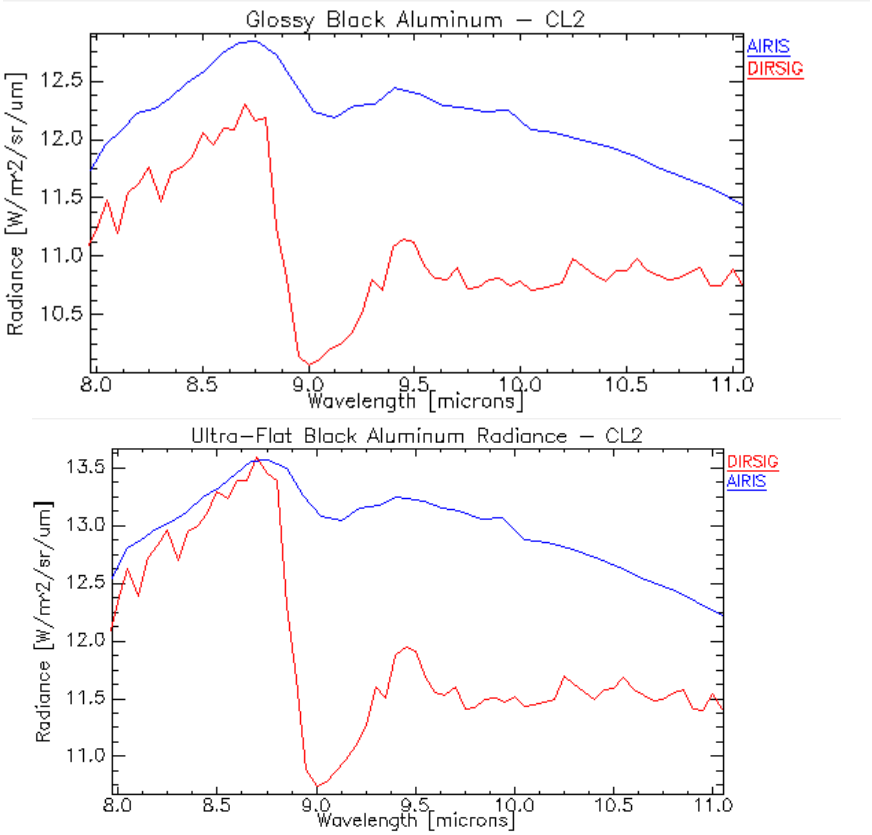

Figure 5.16: Estimated spectral radiance obtained from AIRIS DIRSIG simulation for ultra-flat black and glossy black aluminum samples with CL2. Sample emissivity was defined using uDIRSIG 75 off-nadir model output and temperature of sample was set to retrieved temperature obtained from TES algorithm

Chapter 6

Summary and Future Work

6.1 Summary

The objective of this these to verify and validate predicted infrared spectra from a recently developed radiative transfer model through the use of empirical measurements. This model, known as microDIRSIG, is a physics based reverse ray tracing model that outputs a bidirectional reflectance distribution function of a microfacetized surface. The application of this work was to provide validation for surfaces that had the presence of a liquid contaminant. An experiment was designed to test model outputs of a variety of different substrates to empirically measured data obtained from Fourier transform infrared spectrometers.

This experiment included aluminum and wood substrates with different paint finishes and different levels of contamination. Within the modeling, the contaminant was defined as a thin film, which was assumed homogeneous. The results in chapter 5 showed a promising agreement between the microDIRSIG outputs and the the D&P model 102 measurements for surfaces that were indeed homogeneous. With the exception of the bare aluminum samples, all other aluminum sample model predictions were well within the error bounds of the measurements, thus validating the model for homogeneous surfaces.

Microscopic images of the surfaces were used to validate the homogeneous assumptions for each substrate. A subset of the substrates, particular the wood surfaces did contain spatial non uniformity that was visible within the microscopic images. This non uniformity was a combination of the paint finish as well as the contaminant interaction within varying grain distributions on the wood surface. The spatial variance led to a few violations within the assumptions of the model and may have caused the deviation of the modeled results from the measurements. The discrepancies between the modeled and measured spectra lead to several future work opportunities.

6.2 Additional Contaminant and Substrate Combinations

Expanding the amount of contaminant and substrate combinations will greatly help with the model validation. This work focused primarily on a single contaminant (SF96) along with two primary substrates (wood and aluminum) with three different paint finishes and three different contaminant amounts. While eighteen substrate and contaminant combinations may seem cumbersome and sufficient for validation, the spectra from sample to sample did not vary greatly. In the application of detecting liquid contaminants in realistic scenarios, the range of substrates may be expanded to include asphalt, concrete, or building materials. The range of contaminant may also be expanded to include other liquid contaminates such as DEP. A wider array of contamination cases may lead to a more comprehensive validation.

6.3 Quantifying Contaminants on Surfaces

The aluminum was smooth and meant to provide a simple case where the contaminant would rest as a homogeneous thin film that could be well characterized geometrically. The wood substrate offered more complexity due to slight surface roughness and slight non-uniformity with respect to the wood grain distribution. This non-uniformity added

difficulty in geometrically defining the contaminant within the modeling. The contaminant also non-uniformly absorbed into the wood as opposed to resting as a thin film. The film thickness on the surface was therefore difficult to approximate and provided an uncertain input within microDIRSIG.

The thickness of the contaminant layer in this research was approximated by applying a known contaminant weight of a known density onto a specified area. This method is accurate for non porous surfaces such as aluminum or steel where the contaminant rests as a thin homogeneous film on the surface. This method may fail for porous surfaces such as asphalt or sand where the contaminant may infiltrate through a surface leading to complexities and non linearity when defining a contaminant amount on a surface. The thickness of the contaminant layer may also spatially vary depending on surface roughness or cause an unmixing problem where parts of the bare substrate are exposed. Future work could involve developing a better methodology for geometrically defining a contaminant on a surface. Being able to replicate the measured scene geometrically in the modeling world is very important for developing accurate simulations of the scene.

6.4 Modeling Heterogeneous Surfaces

Another area of future work is modeling heterogeneous substrates. This work provided results for wood and aluminum substrates that had a homogeneous paint finish on the surface. Aggregate materials such as asphalt, concrete, and sand may contain any combination of loosely packed or different sized mass fragments. These types of surfaces are often found in real world scenarios and much more complex to model. Future model validation for the application of chemical detection in a real world cluttered background is highly desired. Improving surface modeling of aggregate or heterogeneous surfaces can lead to advances and improvements in detecting and characterizing liquid contaminants.

Appendices

Appendix A

Additional Measurements

A few other substrate contaminant cases were measured, however they were not used for model validation. These plots are meant to sugest future work in the model validation. The weathered brick and asphalt surfaces with SF96 are more complex and realistic surfaces. Asphalt, in particular is an aggregate substrate that has a spatially varying surface in both roughness and material. The contaminant levels for asphalt substrates correspond to clean, $50\frac{\mu g}{cm^2}$, and $100\frac{\mu g}{cm^2}$. For the brick substrates, each contaminant layer is represented by number of sprays. Prior to applying the contaminant, the attributes of the spray bottle such as weight per spray and diameter of spray projection were measured. Each spray repeatably weighed approximatly 0.13 grams and the spray diameter from a distance of about 12 inches from the sample was approximately 4 inches. The brick measurements were taken from nadir at a path length of about 12 inches which resulted in a spot size of about 1 inch which was well within the boundaries of the contaminant.

Figure A.1: Picture of weathered asphalt sample with SF96 applied

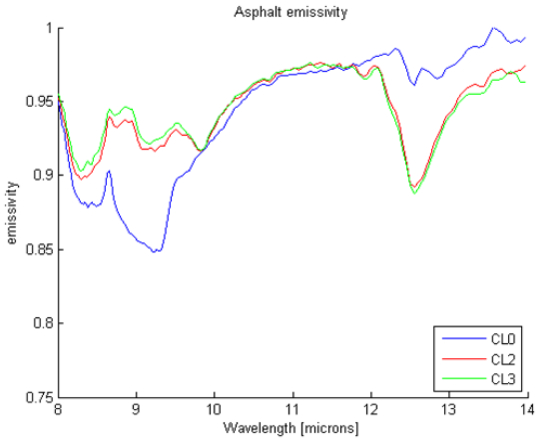

Figure A.2: Emissivity of weathered asphalt with SF96 contaminant

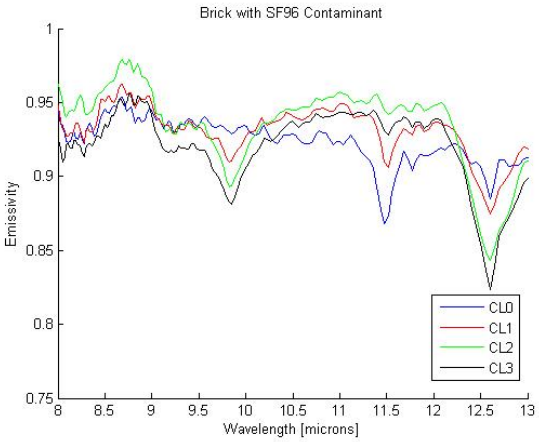

Figure A.3: Emissivity of brick with different amounts of SF96 applied

Appendix B

Thermal Drift Code

This code was implemented into a D&P FTIR calibration graphical user interface coded by Carl Salvaggio. If the user checks the "interpolate blackbody curves" option, the code is initiated and will find the closest blackbody measurements that envelope the sample time to perform a linear time interpolation. The newly generated pseudo blackbody curves are then used to create the calibrated radiance files.

```
FUNCTION int_bb_curves, Int_time, $
  CBBSPECTRUM=cbbspectrum, $
  WBBSPECTRUM=wbbspectrum


cbb_files = FILE_SEARCH$
        ('C:\Users\sean\documents\GRA_LWIR\Andover2014\*.cbb')
cbb_times = MAKE_ARRAY(N_ELEMENTS(cbb_files),1,VALUE=0)
FOR i = 0,N_ELEMENTS(cbb_files)-1 DO BEGIN
  temp = SYSTIME(0,(FILE_INFO(cbb_files[i])).mtime)
  hour = STRMID(temp,11,2)
  minute = STRMID(temp,14,2)
```

```
   cbb_times[i] = hour*60+minute
ENDFOR

wbb_files = FILE_SEARCH$
        ('C:\Users\sean\documents\GRA_LWIR\Andover2014\*.wbb')
wbb_times = MAKE_ARRAY(N_ELEMENTS(wbb_files),1,VALUE=0)
FOR i = 0,N_ELEMENTS(wbb_files)-1 DO BEGIN
   temp = SYSTIME(0,(FILE_INFO(wbb_files[i])).mtime)
   hour = STRMID(temp,11,2)
   minute = STRMID(temp,14,2)
   wbb_times[i] = hour*60+minute
ENDFOR

FOR i = 0,N_ELEMENTS(cbb_times)-2 DO BEGIN
   IF ( Int_time GT cbb_times[i] ) $
    AND ( Int_time LT cbb_times[i+1]) THEN BEGIN
      time_low = i
      time_high = i+1
     BREAK
   ENDIF
ENDFOR

red   = [ 0, 1, 0, 0, 1, 1, 0, 1 ]
green = [ 0, 0, 1, 0, 1, 0, 1, 1 ]
blue  = [ 0, 0, 0, 1, 0, 1, 1, 1 ]

DEVICE, DECOMPOSED=0
```

```
TVLCT, 255*red, 255*green, 255*blue

FOR i = 0,N_ELEMENTS(cbb_files)-1 DO BEGIN
  read_dp_file, cbb_files[i], $
    '102', header=cbb1header, spectrum=cbb1spectrum
    IF i EQ 0 THEN BEGIN
      WINDOW, 0
      plot, cbb1spectrum.wavelength, $
        cbb1spectrum.value, $
        TITLE='Cold Blackbody', $
        XTITLE='Wavelength (microns)', $
        YTITLE='DC', $
        COLOR=7, $
        XRANGE=[0,20], $
        BACKGROUND=0, $
        /NODATA
    ENDIF ELSE BEGIN
    OPLOT, cbb1spectrum.wavelength, $
      cbb1spectrum.value, $
      COLOR=1
    ENDELSE
ENDFOR

FOR i = 0,N_ELEMENTS(wbb_files)-1 DO BEGIN
  read_dp_file, wbb_files[i], $
    '102', header=wbb1header, spectrum=wbb1spectrum
  IF i EQ 0 THEN BEGIN
```

```
    WINDOW, 1
    plot, wbb1spectrum.wavelength, $
      wbb1spectrum.value, $
      TITLE='Warm Blackbody', $
      XTITLE='Wavelength (microns)', $
      YTITLE='DC', $
      COLOR=7, $
      XRANGE=[0,20], $
      BACKGROUND=0, $
      /NODATA
  ENDIF ELSE BEGIN
    OPLOT, wbb1spectrum.wavelength, $
      wbb1spectrum.value, $
      COLOR=1
  ENDELSE
ENDFOR



read_dp_file, cbb_files[time_low], $
  '102', header=cbb1header, spectrum=cbb1spectrum
read_dp_file, cbb_files[time_high], $
  '102', header=cbb2header, spectrum=cbb2spectrum
read_dp_file, wbb_files[time_high], $
  '102', header=wbb1header, spectrum=wbb1spectrum
read_dp_file, wbb_files[time_high], $
  '102', header=wbb2header, spectrum=wbb2spectrum
```

```
cbb_array = [TRANSPOSE(cbb1spectrum.value), $
  TRANSPOSE(cbb2spectrum.value)]

wbb_array = [TRANSPOSE(wbb1spectrum.value), $
  TRANSPOSE(wbb2spectrum.value)]

spectrumSize = N_ELEMENTS(cbb1spectrum.wavelength)

cbbspectrum = { WAVELENGTH:FLTARR(spectrumSize), $
  VALUE:FLTARR(spectrumSize) }

wbbspectrum = { WAVELENGTH:FLTARR(spectrumSize), $
  VALUE:FLTARR(spectrumSize) }

Int_cold_BB = MAKE_ARRAY(N_ELEMENTS(cbb1spectrum.wavelength),1, $
  VALUE = 0.0)
Int_warm_BB = MAKE_ARRAY(N_ELEMENTS(wbb1spectrum.wavelength),1, $
  VALUE = 0.0)

FOR i = 0,N_ELEMENTS(cbb1spectrum.wavelength)-1 DO BEGIN
  Int_cold_BB[i] = CAL_INTERP(cbb_array[*,i], $
    cbb_times[time_low:time_high], $
    Int_time)
  Int_warm_BB[i] = CAL_INTERP(wbb_array[*,i], $
    wbb_times[time_low:time_high], $
    Int_time)
ENDFOR
```

```
cbbspectrum.wavelength = cbb1spectrum.wavelength
wbbspectrum.wavelength = wbb1spectrum.wavelength
cbbspectrum.value = Int_cold_BB
wbbspectrum.value = Int_warm_BB

RETURN, [[cbbspectrum], [wbbspectrum]]



FUNCTION CAL_INTERP, data, BB_times, Int_time

p = POLY_FIT(BB_times,data,1)
result = p(1)*Int_time+p(0)

RETURN, result

END
```

Appendix C

Error Propagation

This code was implemented in MATLAB by utilizing symbolic variables and the diff command. The flow chart of this function is presented in 4.11. The inputs are a file name for writing the results to, the interpolation time, the raw instrument counts as a .txt file, and the temperature.

```
function out = error_prop(file_name,int_time,Vs1,T)
%% INPUTS
% plot_title = 'Bare Aluminum - 50 ug/cm^2 SF96 Error';
% int_time = 77;    % TIME OF SAMPLE
% Vs1 = load('gl_alum_sf96_50_2.sam.txt');    %SAMPLES
% %Vs2 = load('gl_alum_sf96_50_2.sam.txt');
% T = 55.3+273;    %TEMPERATURE OF SAMPLE 45
% file_name = ...
% 'C:\Users\sean\Documents\GRA_LWIR\Final_Curves\gl_alum_rad.txt';
% BB calibration

syms Th Tc S_l S_T c1 c2 lam
```

```
% Planck Function

% Warm BB
Lbbh = (c1/lam^5/(exp(c2/lam/Th)-1))/pi;
d_Lbbh_lam = diff(Lbbh,lam);
d_Lbbh_T = diff(Lbbh,Th);
S_Lbbh = ((d_Lbbh_lam*S_l)^2+(d_Lbbh_T*S_T)^2)^(1/2);

% Cold BB
Lbbc = (c1/lam^5/(exp(c2/lam/Tc)-1))/pi;
d_Lbbc_lam = diff(Lbbc,lam);
d_Lbbc_T = diff(Lbbc,Tc);
S_Lbbc = ((d_Lbbc_lam*S_l)^2+(d_Lbbc_T*S_T)^2)^(1/2);

% Instrument precision parameters
Th = 60+273;
Tc = 10+273;
S_l = 0.001;
S_T = 0.1;
c1 = 3.74151e08;
c2 = 1.4387e04;

% INPUT WAVELENGTH
lam = load('wave.txt');

% Evaluate Equation
```

```
S_Lbbh = eval(S_Lbbh);
S_Lbbc = eval(S_Lbbc);
Lbbh = eval(Lbbh);
Lbbc = eval(Lbbc);

% Responsivity of the D&P model 102
syms Vh Vc RLbbh RLbbc S_Vh S_Vc R_S_Lbbh R_S_Lbbc

% Slope
R = (RLbbh-RLbbc)/(Vh-Vc);
d_R_Vh = diff(R,Vh);
d_R_Vc = diff(R,Vc);
d_R_Lbbh = diff(R,RLbbh);
d_R_Lbbc = diff(R,RLbbc);
S_R = ((d_R_Vh*S_Vh)^2+(d_R_Vc*S_Vc)^2+(d_R_Lbbh*R_S_Lbbh)^2+...
        (d_R_Lbbc*R_S_Lbbc)^2)^(1/2);

% INPUT psuedo CALIBRATION CURVES
S_bb = int_bb_err(122.000001);
bb = int_bb(int_time);
Vh = bb(:,1);
Vc = bb(:,2);
Vh(1) = 1;
Vh(2048) = 1;
S_Vh = S_bb(:,1);
S_Vc = S_bb(:,2);
RLbbh = Lbbh;
```

```
RLbbc = Lbbc;
R_S_Lbbh = S_Lbbh;
R_S_Lbbc = S_Lbbc;

R = eval(R);
S_R = eval(S_R);

% Offset
syms L0_Lbbh L0_Vh L0_R L0_S_Lbbh L0_S_Vh L0_S_R

% Y-intercept
L0 = L0_Lbbh-L0_Vh*L0_R;
d_L0_Lbbh = diff(L0,L0_Lbbh);
d_L0_Vh = diff(L0,L0_Vh);
d_L0_R = diff(L0,L0_R);

S_L0 = ((d_L0_Lbbh*L0_S_Lbbh)^2+(d_L0_Vh*L0_S_Vh)^2...
        +(d_L0_R*L0_S_R)^2)^(1/2);

L0_Lbbh = Lbbh;
L0_Vh = Vh;
L0_R = R;
L0_S_Lbbh = S_Lbbh;
L0_S_Vh = S_Vh;
L0_S_R = S_R;

L0 = eval(L0);
```

```
S_L0 = eval(S_L0);

% Conversion to Calibrated Spectral Radiance
syms L_R L_L0 Vh Vc Vs Vd e S_Td Td Ls_S_R Ls_S_L0...
 Ls_S_Vs Ld_S_R Ld_S_L0 Ld_S_Vd

% Sample calibrated spectral radiance
Ls = L_R*Vs+L_L0;
d_Ls_L_R = diff(Ls,L_R);
d_Ls_L_L0 = diff(Ls,L_L0);
d_Ls_Vs = diff(Ls,Vs);

% Downwelled calibrated spectral radiance
Ld = L_R*Vd+L_L0;
d_Ld_L_R = diff(Ld,L_R);
d_Ld_L_L0 = diff(Ld,L_L0);
d_Ld_Vd = diff(Ld,Vd);

S_Ls = ((d_Ls_L_R*Ls_S_R)^2+(d_Ls_L_L0*Ls_S_L0)^2...
        +(d_Ls_Vs*Ls_S_Vs)^2)^(1/2);
S_Ld = ((d_Ld_L_R*Ld_S_R)^2+(d_Ld_L_L0*Ld_S_L0)^2...
        +(d_Ld_Vd*Ld_S_Vd)^2)^(1/2);

% INPUT SAMPLE Instrument counts
S_Vs = abs(Vs1-Vs2);
Vd1 = load('downwell1.txt');
Vd2 = load('down_gl_alum1.txt');
```

```
Vd3 = load('down_fl_alum1.txt');
Vd4 = load('down31.txt');
VD = horzcat(Vd1,Vd2,Vd3,Vd4);
VDt = [26 48 63 126];
timediff = abs(VDt-int_time);
minimum = min(timediff);
ind = find(timediff == minimum);
m_Vd = (Vd1+Vd2+Vd3+Vd4)/4;
Vs = Vs1;
% Vd = VD(:,ind);
Vd = VD(:,4);
S_Vd = abs(m_Vd-Vd);

Ls_S_R = S_R;
Ls_S_L0 = S_L0;
Ls_S_Vs = S_Vs;
Ld_S_R = S_R;
Ld_S_L0 = S_L0;
Ld_S_Vd = S_Vd;
L_R = R;
L_L0 = L0;
Ls = eval(Ls);
Ld = eval(Ld);
S_Ls = eval(S_Ls);
S_Ld = eval(S_Ld);

%plot radiance error
```

```
Rad_error = mean(S_Ls(245:398));

% Downwelled Correction
syms Lpl_lam L_Ld Lpl_S_Ld Lpl_S_Td Lpl_c1 Lpl_c2
Lpl = e*(c1/Lpl_lam^5/(exp(c2/Lpl_lam/Td)-1))/pi;
d_Ld_lam = diff(Lpl,Lpl_lam);
d_Ld_T = diff(Lpl,Td);
S_Lpl = ((d_Ld_lam*Lpl_S_Ld)^2+(d_Ld_T*Lpl_S_Td)^2)^(1/2);

S_Td = 0.01;
Lpl_c1 = c1;
Lpl_c2 = c2;
Lpl_S_Ld = S_Ld;
Lpl_S_Td = S_Td;
Lpl_lam = lam;
L_Ld = Ld;
Td = 30.3+273;
e = 0.02;


Lpl = eval(Lpl);
S_Lpl = eval(S_Lpl);


% Final Downwelled
syms Ldown_Ld Ldown_Lpl e Ldown_S_Ld Ldown_S_Lpl
Ldown = (Ldown_Ld-Ldown_Lpl)/(1-e);
```

```
d_Ldown_Ld = diff(Ldown,Ldown_Ld);
d_Ldown_Lpl = diff(Ldown,Ldown_Lpl);
S_Ldown = ((d_Ldown_Ld*Ldown_S_Ld)^2...
        +(d_Ldown_Lpl*Ldown_S_Lpl)^2)^(1/2);

Ldown_S_Ld = S_Ld;
Ldown_S_Lpl = S_Lpl;
e = 0.02;
Ldown_Ld = Ld;
Ldown_Lpl = Lpl;

Ldown = eval(Ldown);
S_Ldown = eval(S_Ldown);

% Emissivity
syms e_Ls e_Ld e_BB S_Ts e_lam Ts BB_S_Ld BB_S_Ts e_c1 e_c2 e_Ts

BB = (e_c1/e_lam^5/(exp(e_c2/e_lam/Ts)-1))/pi;
d_BB_lam = diff(BB,e_lam);
d_BB_T = diff(BB,Ts);
S_BB = ((d_Ld_lam*BB_S_Ld)^2+(d_Ld_T*BB_S_Ts)^2)^(1/2);

e_c1 = c1;
e_c2 = c2;
BB_S_Ld = S_Ld;
e_Ld = Ld;
e_Ls = Ls;
```

```
e_lam = lam;
S_Ts = 8;
Ts = T;
BB_S_Ts = S_Ts;

BB = eval(BB);
S_BB = eval(S_BB);

syms ee_Ls ee_Ld emiss_S_Ls emiss_S_Ld emiss_S_BB
emiss = (ee_Ls-ee_Ld)/(e_BB-ee_Ld);
d_e_Ls = diff(emiss,ee_Ls);
d_e_Ld = diff(emiss,ee_Ld);
d_e_BB = diff(emiss,e_BB);
S_emiss = ((d_e_Ls*emiss_S_Ls)^2+(d_e_Ld*emiss_S_Ld)^2+...
        (d_e_BB*emiss_S_BB)^2)^(1/2);

emiss_S_Ls = S_Ls;
emiss_S_Ld = S_Ld;
emiss_S_BB = S_BB;
ee_Ls = Ls;
ee_Ld = Ld;
e_BB = BB;

emiss = eval(emiss);
S_emiss = eval(S_emiss);

high = max(find(lam > 8));
```

```
low = min(find(lam < 14));

% figure, hold on
% plot(lam, S_emiss)
% % plot(lam, emiss+S_emiss, 'r-');
% % plot(lam, emiss-S_emiss, 'r-');
% xlim([8 14]);
% title(plot_title)
% xlabel('Wavelength'); ylabel('Emissivity Error')
% legend('Measured Emissivity','RMS Error Deviation','location','southeast')
% hold off

%% WRITE DATA to TEXT FILE
data = [lam'; Ls'; S_Ls'];

fid = fopen(file_name,'w');
fprintf(fid,'%6.4f %6.4f %6.4f \n',data);
fclose(fid);

out = [lam'; emiss'; S_emiss'];
```

Appendix D

DIRSIG FTIR Implementation

This code takes a high resolution radiance output from a DIRSIG or MODTRAN simulation and applies a post interferogram processing algorithm to truncate the result to the D&P FTIR spectral resolution.

```
function out = ftir(rad)
%Radiance output from DIRSIG at 1 wavenumber sampling
rad = double(dlmread('ufb_alum_rad_z20.txt','',3,0));
L = length(rad);
% wn = 10000./rad(:,1);
figure, hold on
subplot(2,3,1)
plot(rad(:,1),rad(:,2))
title('DIRSIG Radiance')
xlabel('Wavenumber [1/cm]'); ylabel('Radiance [w/cm^3/sr]')
xlim([800 1400])

%Inverse fourier transform to produce interferogram
```

```
fftrad = ifftshift(fft(fftshift(rad(:,2))));
% fftwn = ifftshift(fft(fftshift(wn)));
shift = -357:1:357;
subplot(2,3,2), hold on
plot(shift,real(fftrad))
plot(shift,imag(fftrad))
hold off
title('Interferogram');


%Applying Hanning window for D&P apodization
w = hann(round(L/4));
W = padarray(w,floor((L-length(w))/2));
apodization = W.*fftrad;

subplot(2,3,3)
plot(shift,W)
title('Hanning window function')

subplot(2,3,4), hold on
plot(shift,real(apodization))
plot(shift,imag(apodization))
hold off
title('Apodized Interferogram')


%FFT back to wavenumber space
```

```
newrad = fftshift(fft(fftshift(apodization)));
newrad = flipud(newrad/size(fftrad,1));

subplot(2,3,5)
plot(rad(:,1),real(newrad))
title('Final Radiance')
ylabel('Radiance [w/cm^3/sr]'); xlabel('Wavenumber [1/cm]')
xlim([800 1400])

%convert to microns
for i = 1:length(rad(:,1))
    wl1 = 10000/(rad(i,1)-0.5);
    wl2 = 10000/(rad(i,1)+0.5);
    delta_wl = wl1-wl2;
    new_wl(i) = 10000/rad(i,1);
    new_rad(i) = newrad(i)*(1/delta_wl);
end

subplot(2,3,6)
plot(new_wl,new_rad)
title('Predicted Radiance')
xlabel('Wavelength [microns]'); ylabel('Radiance [w/cm^2/sr/um]')
xlim([7.2 12.8])


meas_rad = dlmread('9sf_ufb90.sac',',',1,0);
meas_rad_err = load('fl_wood_rad.txt');
```

```
figure, hold on
h = plot(new_wl(4:705),new_rad(4:705)*10000,'r');
H = shadedErrorBar(meas_rad(:,1),meas_rad(:,2),meas_rad_err(:,3),'b',1);
title('DIRSIG modeled radiance vs Measured Radiance [AL UFB-SF96]')
xlabel('Wavelength [microns]'); ylabel('Radiance [W/m^2/sr/um]')
xlim([8  12.8])
%legend('DIRSIG','D&P FTIR')
legend([H.mainLine H.patch h],{'D&P FTIR','+/- RMS Error','DIRSIG'})
xlim([8  12.8]);

%RMS Error
upper = find(meas_rad(:,1) < 8, 1 );
lower = find(meas_rad(:,1) > 12.5, 1, 'last' );
meas_int = interp1(new_wl,real(new_rad*10000),meas_rad(lower:upper,1));
RMS = sqrt(sum((meas_rad(lower:upper,2)-term-meas_int).^2)...
        /length(meas_int))
SAM = acosd(dot(meas_int,meas_rad(lower:upper,2))...
     /(norm(meas_int)*norm(meas_rad(lower:upper,2))))
```

Bibliography

[1] John R. Schott. Remote Sensing: The Image Chain Approach, Oxford University Press, 1996.

[2] Frank L. Pedrotti, S.J, Leno S. Pedrotti, Leno M. Pedrotti. Introduction to Optics, Third Edition. Pearson Prentice Hall, 2007

[3] James R. Shell PhD Dissertation, Rochester Institute of Technology, Center for Imaging Science, 2005.

[4] F. E. Nicodemus. Reflectance nomenclature and directional reflectance and emissivity. Applied Optics, 9(6):14741475, June 1970.

[5] Michael G. Gartley PhD Dissertation, Rochester Institute of Technology, Center for Imaging Science, 2007

[6] Mark A. Culpepper. Empirical bidirectional reflectivity model. In Targets and Backgrounds: Characterization and Representation, volume 2469 of Proc. SPIE, pages 208219, 1995.

[7] K.E. Torrance and E. M. Sparrow, Theory for off-specular reflection from roughned surfaces, Journal of the Optical Society of America, v57, n9, pages 1105-1114, 1967.

[8] Richard G. Priest and Thomas A. Germer. Polarimetric BRDF in the microfacet model: Theory and measurements. In Proceedings of the 2000 Meeting of the Military Sens-

ing Symposia Specialty Groupon Passive Sensors, volume 1, pages 169181. Infrared Information Analysis Center, Ann Arbor, MI, 2000.

[9] Planck, M. (1914). The Theory of Heat Radiation. Masius, M. (transl.) (2nd ed.). P. Blakiston's Son & Co. OL 7154661M.

[10] William C. Snyder, Zhengming Wan, Yulin Zhang and Yue-Zhong Feng. Thermal Infrared (314 m) Bidirectional Reflectance Measurements of Sands and Soils. Remote Sensing of Environment, 1997, Vol. 60, pp 101-109, 1997.

[11] K. Strackerjan, L. Smith, and J. Kerekes, "Modeling the Spectral Effects of Water and Soil as Surface Contaminants in a High Resolution Optical Image Simulation," Proceedings of the 2006 IEEE International Geoscience and Remote Sensing Symposium (IGARSS), pp. 3757-3760, Denver, Colorado, 2006.

[12] Sharpe, S., Johnson, T., Sams, R., et al., Infrared spectral signatures: Creation of reference data for vapors and liquids, Intl. J. High-Speed Electronics and Systems 18, 231-250 (2008).

[13] Theriault, J. M., Hancock, J., Jensen, J. O., and Puckrin, E., Passive standoff detection of liquid surface contaminants: Recent results with CATSI, Proc. SPIE 5268, 310-320 (2004).

[14] Farley, V., Vallieres, A., Villemaire, A., et al., Chemical agent detection and identification with a hyperspectral imaging infrared sensor, Proc. SPIE 6739, 673918 (2007).

[15] Goyal, A., Spencer, M., Kelly, M., Costa, J. "Active infrared multispectral imaging of chemicals on surfaces," Proc. SPIE 8018, 80180N-1 (2011).

[16] Harig, R., Braun, R., Dyer, C., Howle, C., and Truscott, B., Short-range remote detection of liquid surface contamination by active imaging Fourier transform spectrometry, Opt. Express 16, 5708-5714 (2008).

[17] Born, M.; Wolf, E., Principles of optics: electromagnetic theory of propagation, interference and diffraction of light. Oxford, Pergamon Press, 1964.

[18] M. Gartley, personal communication. January, 2015

[19] J. Kerekes, M. Gartley, C. DeAngelis, C. Salvaggio, C. Gittens, M. Costolo, and B. Cosofret, "Measurements and Modeling of LWIR Spectral Emissivity of Contaminated Quartz Sand," Proceedings of the Fifth IEEE Workshop on Hyperspectral Image and Signal Processing: Evolution in Remote Sensing (WHISPERS), 25-27 June 2013.

[20] J. R. Maxwell, J. Beard, S. Weiner, D. Ladd, and S. Ladd. Bidirectional re- flectance model validation and utilization. Technical Report AFAL-TR-73-303, Environmental Research Institute of Michigan (ERIM), October 1973.

[21] Michael Hazlett, Dennis J. Andersh, Shung W. Lee, Hao Ling and C.L. Yu. XPATCH: a high-frequency electromagnetic scattering prediction code using shooting and bouncing rays, Proceeding of the SPIE, Targets and Backgrounds: Characterization and Representation. Vol. 266. June, 1995

[22] Schlesinger, S. 1979 et al. Terminology for model credibility. Simulation 32 (3): 103-104.

[23] Nonconventional Exploitation Factors Data System (NEFDS) Modeling Document v10, National Geospatial Intelligence Agency (2006).

[24] Alexander Berk et al, MODTRAN: A Moderate Resolution Model for LOWTRAN 7, Air Force Geophysics Lab, GL-TR-89-C122, April 1989.

[25] Gartley, M., Brown, S., and Schott, J., Polarimetric scene modeling in the thermal infrared, Proc. of SPIE, Polarization Science and Remote Sensing III 6682 (2007).

[26] D$P Instruments, Model 102 Win2K Instruction Manual, Ver. 1.2, May 2006

[27] C. Salvaggio, C. Miller, R. Bauer, P. Lewis. Infrared Field Spectra Collection Protocol, Spectral Information Technology Applications Center. November, 2000.

[28] K. Horton, J. Johnson, P. Lucey. Infrared measurements of pristine and disturbed soils 2. Environmental effects and field data reduction. Remote Sensing Environment. Vol. 64, pp. 47-52, 1998

[29] R. Kitamura, L. Pilon, M. Jonasz. Optical constants of silica glass from extreme ultraviolet to far infrared at near room temperature. Applied Optics. Vol. 46, pp. 8118-8133, 2007

[30] Beers, Y. (1957). Introduction to the Theory of Errors. addison-Wesley, Reading, MA

[31] W. Marinelli, C. Gittins, B. Cosofret, T. Ustun. "Development of the AIRIS-WAD Multispectral Sensor for Airborne Standoff Chemical Agent and Toxic Industrial Chemical Detection". presented at 2005 Parallel Meetings of the MSS Specialty Groups on Passive Sensors; Camouflage, Concealment, and Deception; Detectors; and Materials (Charleston, SC), (14-18 February, 2005).

[32] M. Querry, Optical constants of minerals and other materials from the millimeter to the ultraviolet, Chemical Research, Development and Engineering Center, University of Missouri-Kansas City, November 1987.

[33] L. Smith, C. Salvaggio, G. DiFrancesco, P. Martinson. Laboratory MWIR/LWIR Collection Protocol, Digital Earth and Remote Sensing Laboratory. August, 2005

[34] J. Beutel. An improved differentiating filter function for computing line spread functions in MTF calculations. Proc. of SPIE, Medical Imaging IV: Image Formation. Vol. 1231, 1990.